

# Topological Mod(A)Max AdS black holes

B. Eslam Panah \*

*Department of Physics, University of Mazandaran, Babolsar, Iran*

B. Hamil †

*Laboratoire de Physique Mathématique et Physique Subatomique, LPMPS,  
Faculté des Sciences Exactes, Université Constantine 1, Constantine, Algeria*

Manuel E. Rodrigues ‡

*Faculdade de Física, Programa de Pós-Graduação em Física,  
Universidade Federal do Pará, 66075-110, Belém, Pará, Brazil  
Faculdade de Ciências Exatas e Tecnologia, Universidade Federal do Pará,  
Campus Universitário de Abaetetuba, 68440-000, Abaetetuba, Pará, Brazil*

In this work, we construct new classes of topological black hole solutions in anti-de Sitter (AdS) spacetime using a novel model of nonlinear electrodynamics called Modification Maxwell (ModMax) and Modification phantom or Modification anti-Maxwell (ModAMax). We then evaluate the thermodynamic quantities and verify the first law of thermodynamics. Our study examines how the parameters of the ModMax and ModAMax fields, as well as the topological constant, affect the black hole solutions, thermodynamic quantities, and local and global thermal stabilities. Furthermore, within the framework of extended phase space thermodynamics, we analyze the Joule-Thomson expansion process and determine the inversion curves. This analysis reveals that the ModMax and ModAMax parameters significantly alter the cooling and heating behavior of these AdS black holes, depending on their topology. Finally, by treating these topological Mod(A)Max AdS black holes as heat engines, we assess their efficiencies, demonstrating that the parameters of nonlinear electrodynamics and horizon topology play crucial roles in enhancing or suppressing the system's thermodynamic performance.

## I. INTRODUCTION

Within the realm of physics, one occasionally encounters systems whose behavior defies ordinary expectations, displaying negative energy densities. Such configurations appear in several distinct contexts [1]. Among the best-known are: (a) the traditional Casimir effect, observed between two uncharged parallel plates as well as in its topological extension; (b) the squeezed vacuum state, which emerges in quantum optics; (c) the Hartle–Hawking vacuum, a quantum state relevant to black hole thermodynamics; and (d) the so-called phantom field, a hypothetical entity invoked to explain the accelerated expansion of the cosmos [2].

Comparable scenarios arise within the framework of gravitation. A historically important instance is the quasi-charged bridge introduced by Einstein and Rosen in 1935 [3]. In that construction, the system acquires an effective electric charge with an inverted sign relative to the Reissner–Nordstrom geometry, expressed formally as ( $q^2 \rightarrow -q^2$ ). This feature effectively introduces into the action the first manifestation of a spin-1 phantom field, characterized by its negative energy contribution.

Phantom fields are not limited to vector forms. The anti-Fisher solution [4] provides a notable example of a scalar, or spin-0, phantom configuration. When scalar and electromagnetic phantom components are coupled, the resulting models are known as Einstein-anti-Maxwell-anti-Dilaton systems [5]. Various extensions of these models have been developed, including those incorporating a cosmological constant [6], as well as regular configurations free from singularities [7]. The Sigma-model approach has also been employed to construct rotating phantom solutions [8].

The study of phantom and related systems has expanded considerably, encompassing analyses of photon trajectories [9], gravitational collapse [10], lensing phenomena [11], global monopoles [12], quasi-black holes [13], dyonic black holes [14], wormhole geometries [15], spherical accretion processes [16], topological black holes within  $f(R)$  gravity [17], and, more recently, the intriguing class of black–bounce spacetimes [18].

---

\*Electronic address: eslampanah@umz.ac.ir

†Electronic address: hamilbilel@gmail.com/bilel.hamil@umc.edu.dz

‡Electronic address: esialg@gmail.com

Linear Maxwell electrodynamics possesses a remarkably elegant structure. It is invariant under the  $U(1)$  gauge group and is governed by second-order, linear differential equations in the electromagnetic potentials. These features ensure both mathematical simplicity and physical consistency. However, when such assumptions are relaxed, a variety of richer and more exotic behaviors emerge that are absent in the linear theory.

If the  $U(1)$  gauge symmetry is broken, the resulting field equations generally become of higher order in the potentials, as exemplified in the formulations of Podolsky and Proca electrodynamics [19–21]. On the other hand, allowing for nonlinear dependencies in the electromagnetic field invariants gives rise to entire families of modified theories collectively known as nonlinear electrodynamics (NED). Such frameworks predict novel physical effects, including magnetic birefringence, in which light propagates anisotropically—its velocity depending on both the orientation of the external magnetic field and the direction of the light’s polarization [22].

The origins of NED trace back to Born and Infeld in 1934 [23], who sought to eliminate the divergent self-energy of point charges inherent in Maxwell’s formulation. Their theory successfully regularized the field energy near charged particles, thereby removing the singularity at the charge’s position. A few years later, in 1936, Euler and Heisenberg developed a quantum-field-based form of NED to describe photon–photon scattering [24]. Soon after, Hoffmann extended the Born–Infeld Lagrangian to include gravitational coupling [25], establishing the foundation for subsequent studies in NED within curved spacetime.

Since then, NEDs have been invoked across a wide range of physical scenarios, including the ionisation of the hydrogen atom [26], baryogenesis [27], cosmic microwave background polarisation [28], multiple refraction phenomena [29], neutrino astrophysics [30], unidirectional light propagation [31], pulsar emission models [32], cosmological inflation [33], photon gas thermodynamics [34], and the accelerated expansion of the Universe [35].

Experimental exploration of NED effects has been an active and rapidly advancing field. Laboratory tests include the PVLAS (Polarizzazione del Vuoto by LASERS) experiment [36], LSW (Light Shining through Walls) [37], BMV (Birefringence Magnétique du Vide, Toulouse) [38], VH (Vacuum Hohlraum, photon collider) [39], XFELS (X-ray Free Electron LASERS) [40], ELI (Extreme Light Infrastructure) [41], and SULF (Shanghai Ultra-Laser Facilities) [42]. Forthcoming facilities—the Station of Extreme Light (SEL) in Shanghai, expected to operate in 2025, and the ExaWatt Centre for Extreme Light Studies (XCELS) in Russia, anticipated for 2026—may provide decisive experimental confirmation of NED effects.

In 2020, a new model of NED was proposed, retaining the same symmetries as Maxwell’s theory [43, 44]. This model is known as the Modification of Maxwell (ModMax) theory. The ModMax theory is characterized by a dimensionless parameter  $\gamma$ , referred to as the ModMax parameter, which reduces to Maxwell’s theory when  $\gamma = 0$ . Research has examined magnetic [45] and electromagnetized black holes [46] in the presence of ModMax theory. Additionally, various black hole solutions, including accelerating [47–49] and BTZ [50] black holes, have been derived from ModMax theory. The impact of the ModMax parameter on several black hole properties has also been investigated, including shadow [51], quasinormal modes [51, 52], greybody radiation [51], light propagation [53], thermodynamic topology [54], emission rates [52], and gravitational lensing [55]. Moreover, the combination of ModMax with other modified theories of gravity, such as  $F(R)$  [56], massive [57], and Kalb–Ramond [58–60] theories, has led to the exploration of new black hole solutions and their properties. In this regard, further studies on the intriguing aspects of ModMax theory are evaluated in Refs. [61–83].

On the other hand, the topology of the event horizon of a four-dimensional asymptotically flat stationary black hole is uniquely characterized as a two-sphere, denoted as  $S^2$  [84, 85]. This determination is derived from Hawking’s theorem, which asserts that the integrated Ricci scalar curvature, computed with respect to the induced metric on the event horizon, must be positive [84]. However, in spacetimes that do not exhibit asymptotic flatness, the spherical topology of the black hole’s horizon is not mandated; stationary black holes can manifest nontrivial topologies. It has been discussed that in four-dimensional Einstein theory coupled with a Maxwell field, asymptotically AdS spacetimes may possess black hole solutions whose event horizons can exhibit zero or negative constant curvature, resulting in topologies that deviate from the two-sphere  $S^2$  [86–94].

Bekenstein and Hawking identified an analogy between the geometric properties of black holes and thermodynamic variables, enhancing our understanding of the connection between gravity and classical thermodynamics [95]. The thermodynamic properties of black holes, especially phase transitions and thermal stability, are crucial as they provide insights into the fundamental structure of spacetime geometry. Phase transitions are significant across various fields, including elementary particles [96], classical thermodynamics [97], condensed matter [98], black holes [99], and cosmology [100]. An intriguing aspect of black hole thermodynamics is the phase transition occurring in anti-de Sitter (AdS) spacetime, which is informed by AdS/CFT duality [101, 102] and sheds light on the quantum nature of gravity. Recently, the study of phase transitions in AdS black holes within an extended phase space has garnered considerable attention. In this context, the cosmological constant is treated as a variable, recognized as thermodynamic pressure [103], while the mass of the black hole is

interpreted as enthalpy [104].

Recent advances in black hole thermodynamics include the Joule–Thomson (JT) expansion [105] and the development of holographic heat engines [106]. The JT expansion has been applied to black holes in AdS spacetime, inspired by the established analogy between AdS black holes and van der Waals fluids. In classical thermodynamics, JT process describes the expansion of a gas from a region of high pressure to one of low pressure through a porous medium, during which the enthalpy remains constant. This process is inherently adiabatic and isoenthalpic, providing a useful framework for analyzing the thermal behavior of thermodynamic systems. In this context, the JT expansion has been utilized as an isoenthalpic tool to explore the heating and cooling characteristics of black holes. The first detailed investigation of the JT expansion in relation to black holes was reported in [105]. More recently, the JT expansion has been extended to various black hole solutions, including quintessence AdS black holes [107], charged AdS black holes in arbitrary dimensions [108], Kerr-AdS black holes [109], Kerr-Newman-AdS black holes [110], Gauss-Bonnet AdS black holes [111], black holes in Lovelock gravity [112], and black holes in NED [113]. Additionally, C. V. Johnson introduced the concept of a conventional heat engine into black hole thermodynamics. By defining a closed cycle in the pressure-volume ( $P - V$ ) plane for a charged AdS black hole, he demonstrated that useful mechanical work can be extracted from its heat energy [106]. This approach revealed that mechanical work can be derived from the heat energy of both static and stationary AdS black holes, unlike the Penrose process, which is limited to rotating black holes but can occur in both AdS and flat spacetimes. Furthermore, Johnson proposed that black hole heat engines might have intriguing holographic interpretations, as the thermodynamic cycle can be seen as a trajectory through a family of holographically dual large- $N$  field theories [106]. This concept has since garnered significant attention and has been extended to numerous other black hole configurations [114–123].

These studies prompt us to investigate topological AdS black holes with modified Maxwell and phantom (anti-Maxwell) fields. Our goal is to examine how the parameters of these modifications, along with the topological constant, affect black hole solutions, thermodynamic quantities, and the efficiency of heat engines when these black holes are treated as heat engine machines.

## II. MODMAX AND MODAMAX THEORY AND TOPOLOGICAL BLACK HOLE SOLUTIONS

The action describing the coupling of Einstein’s gravity with the cosmological constant in the presence of the Mod(A)Max electrodynamic fields is expressed as

$$\mathcal{I} = \frac{1}{16\pi} \int_{\partial\mathcal{M}} d^4x \sqrt{-g} [R - 2\Lambda - 4\eta\mathcal{L}], \quad (1)$$

where  $g = \det(g_{\mu\nu})$  is the determinant of the metric tensor  $g_{\mu\nu}$ . Also,  $\Lambda$  and  $R$  are related to the cosmological constant and the Ricci scalar, respectively. In addition,  $\eta = +1$ , and  $\eta = -1$  are related to Maxwell and anti-Maxwell (phantom) cases, respectively. It is notable that, Mod(A)Max devotes to both ModMax and ModAMax fields. In other words, Mod(A)Max is related to ModMax field when  $\eta = +1$  or the ModAMax field when  $\eta = -1$ . In the action (1),  $\mathcal{L}$  refers to ModMax’s Lagrangian and is defined as [43, 44]

$$\mathcal{L} = \mathcal{S} \cosh \gamma - \sqrt{\mathcal{S}^2 + \mathcal{P}^2} \sinh \gamma, \quad (2)$$

where  $\gamma$  is known as ModMax’s parameter,. This parameter is a dimensionless quantity. Furthermore,  $\mathcal{S}$  and  $\mathcal{P}$  represent a true scalar and a pseudoscalar, respectively, in the following expressions

$$\mathcal{S} = \frac{\mathcal{F}}{4}, \quad \& \quad \mathcal{P} = \frac{\tilde{\mathcal{F}}}{4}, \quad (3)$$

in the equations above, the term  $\mathcal{F} = F_{\mu\nu}F^{\mu\nu}$  is referred to as the Maxwell invariant. Moreover,  $F_{\mu\nu}$  represents the electromagnetic tensor field and is defined as  $F_{\mu\nu} = \partial_\mu A_\nu - \partial_\nu A_\mu$ , with  $A_\mu$  being the gauge potential. Also,  $\tilde{\mathcal{F}} = F_{\mu\nu}\tilde{F}^{\mu\nu}$ , where  $\tilde{F}^{\mu\nu} = \frac{1}{2}\epsilon_{\mu\nu}^{\rho\lambda}F_{\rho\lambda}$ . By considering  $\gamma = 0$ , the Lagrangian of ModMax (Eq. (2)) reduces to the Maxwell theory as  $\mathcal{L} = \frac{\mathcal{F}}{4}$ .

In order to get electrically charged black holes solutions, we set  $\mathcal{P} = 0$  in the Lagrangian of ModMax (Eq. (2)). So, the generalized Einstein- $\Lambda$  equations in the presence of the modification Maxwell (ModMax) and the modification anti-Maxwell (ModAMax) fields write in the following form [61]

$$G_{\mu\nu} + \Lambda g_{\mu\nu} = 8\pi T_{\mu\nu}, \quad (4)$$

$$\partial_\mu \left( \sqrt{-g} \tilde{E}^{\mu\nu} \right) = 0, \quad (5)$$

where  $T_{\mu\nu}$  is the energy-momentum tensor in the presence of Mod(A)Max field which is given by

$$8\pi T^{\mu\nu} = 2\eta (F^{\mu\sigma}F_{\sigma}^{\nu}e^{-\gamma}) - 2\eta e^{-\gamma}Sg^{\mu\nu}, \quad (6)$$

and  $\tilde{E}_{\mu\nu}$  is defined as

$$\tilde{E}_{\mu\nu} = \frac{\partial \mathcal{L}}{\partial F^{\mu\nu}} = 2(\mathcal{L}_S F_{\mu\nu}), \quad (7)$$

where  $\mathcal{L}_S = \frac{\partial \mathcal{L}}{\partial S}$ .

For charged case, the equation (5), turns to

$$\partial_{\mu} (\sqrt{-g}e^{-\gamma}F^{\mu\nu}) = 0. \quad (8)$$

We consider a topological four-dimensional static metric as

$$ds^2 = -f(r)dt^2 + \frac{dr^2}{f(r)} + r^2d\Omega_k^2, \quad (9)$$

where  $f(r)$  is the metric function, which we are going to extract it. In addition,  $d\Omega_k^2$  is given by

$$d\Omega_k^2 = \begin{cases} d\theta^2 + \sin^2\theta d\varphi^2 & k = 1 \\ d\theta^2 + d\varphi^2 & k = 0 \\ d\theta^2 + \sinh^2\theta d\varphi^2 & k = -1 \end{cases}. \quad (10)$$

Applying the following gauge potential, we can have a radial electric field

$$A_{\mu} = h(r)\delta_{\mu}^t, \quad (11)$$

and using the metric (9) and the equation (8), we find the following relation

$$2h'(r) + rh''(r) = 0, \quad (12)$$

where the prime and double prime are, respectively, the first and second derivatives with respect to  $r$ . By solving the equation (12), we obtain

$$h(r) = -\frac{q}{r}, \quad (13)$$

where  $q$  is an integration constant related to the electric charge.

To extract the metric function,  $f(r)$ , we investigate the equations (4), (6), (9), and (13). We obtain the following differential equations

$$eq_{tt} = eq_{rr} = rf'(r) + f(r) + \Lambda r^2 - k + \frac{\eta q^2 e^{-\gamma}}{r^2} = 0, \quad (14)$$

$$eq_{\theta\theta} = eq_{\varphi\varphi} = f''(r) + \frac{2}{r}f'(r) + 2\Lambda - \frac{2\eta q^2}{r^4}e^{-\gamma} = 0, \quad (15)$$

which  $eq_{tt}$ ,  $eq_{rr}$ ,  $eq_{\theta\theta}$ , and  $eq_{\varphi\varphi}$  are representative  $tt$ ,  $rr$ ,  $\theta\theta$ , and  $\varphi\varphi$  components of Eq. (4), respectively. Applying the differential equations (14) and (15), we can obtain an exact solution for the metric function in the following form

$$f(r) = k - \frac{m}{r} - \frac{\Lambda r^2}{3} + \frac{\eta q^2 e^{-\gamma}}{r^2} = \begin{cases} k - \frac{m}{r} - \frac{\Lambda r^2}{3} + \frac{q^2 e^{-\gamma}}{r^2}, & \text{ModMax} \\ k - \frac{m}{r} - \frac{\Lambda r^2}{3} - \frac{q^2 e^{-\gamma}}{r^2}, & \text{ModAMax} \end{cases}, \quad (16)$$

where  $m$  is an integration constant that is related to the geometrical mass of the black hole. Also, the metric function (16) satisfies all the components of the field equation (4), simultaneously. It is notable that,  $\eta = +1$  belongs to the ModMax solution and  $\eta = -1$  is related to the ModAMax solution. Moreover, the metric function Eq. (16) turns to topological Reissner-Nordstrom AdS black hole when  $\gamma = 0$ , and  $\eta = +1$ , i.e.

$$f(r) = k - \frac{m}{r} - \frac{\Lambda r^2}{3} + \frac{q^2}{r^2}. \quad (17)$$

and for  $\gamma = 0$ , and  $\eta = -1$ , the metric function Eq. (16) reduces to topological anti-Maxwell (phantom) AdS black hole, i.e.

$$f(r) = k - \frac{m}{r} - \frac{\Lambda r^2}{3} - \frac{q^2}{r^2}. \quad (18)$$

We study the Kretschmann scalar to find the singularity of the metric function (16). In this regard, we consider the metric (9) and the metric function (16), and calculate the Kretschmann scalar which leads to

$$\begin{aligned} R_{\alpha\beta\gamma\delta}R^{\alpha\beta\gamma\delta} &= \frac{8\Lambda^2}{3} + \frac{12m^2}{r^6} - \frac{48m\eta q^2 e^{-\gamma}}{r^7} + \frac{56\eta^2 q^4 e^{-2\gamma}}{r^8} \\ &= \begin{cases} \frac{8\Lambda^2}{3} + \frac{12m^2}{r^6} - \frac{48m\eta q^2 e^{-\gamma}}{r^7} + \frac{56\eta^2 q^4 e^{-2\gamma}}{r^8}, & \text{ModMax} \\ \frac{8\Lambda^2}{3} + \frac{12m^2}{r^6} + \frac{48m\eta q^2 e^{-\gamma}}{r^7} + \frac{56\eta^2 q^4 e^{-2\gamma}}{r^8}, & \text{ModAMax} \end{cases}, \end{aligned} \quad (19)$$

which diverges at  $r = 0$  (i.e.,  $\lim_{r \rightarrow 0} R_{\alpha\beta\gamma\delta}R^{\alpha\beta\gamma\delta} \rightarrow \infty$ ). This reveals that, there is a curvature singularity located at  $r = 0$ . In addition, the Kretschmann scalar is finite for  $r \neq 0$ .

The asymptotic behavior of spacetime is determined by

$$\begin{aligned} \lim_{r \rightarrow \infty} R_{\alpha\beta\gamma\delta}R^{\alpha\beta\gamma\delta} &\rightarrow \frac{8\Lambda^2}{3}, \\ \lim_{r \rightarrow \infty} f(r) &\rightarrow -\frac{\Lambda r^2}{3}, \end{aligned} \quad (20)$$

where indicates that the spacetime will be asymptotically de sitter (dS) when  $\Lambda > 0$ , or anti-de Sitter (AdS) when  $\Lambda < 0$ .

We aim to study the effects of the Mod(A)Max parameters ( $\gamma$  and  $\eta$ ) and the topological constant  $k$  on the derived metric function (Eq. 16). To illustrate this, we plot  $f(r)$  versus  $r$  in Figs. 1 to 4. Our findings are as follows:

**ModMax field ( $\eta = +1$ ):** The effect of topological constant reveals that smaller black holes are associated with a positive topological constant ( $k = +1$ ), while larger black holes correspond to a negative topological constant ( $k = -1$ ), see the left panel of Fig. 1. We identify two roots, one corresponding to the inner horizon and the other to the event horizon. In addition, the number of roots varies with the parameter  $\gamma$  (see the left panels in Figs. 2-4). Notably, for sufficiently large values of  $\gamma$ , only a single root exists (see the dotted-dashed line in the left panels in Figs. 2 to 4).

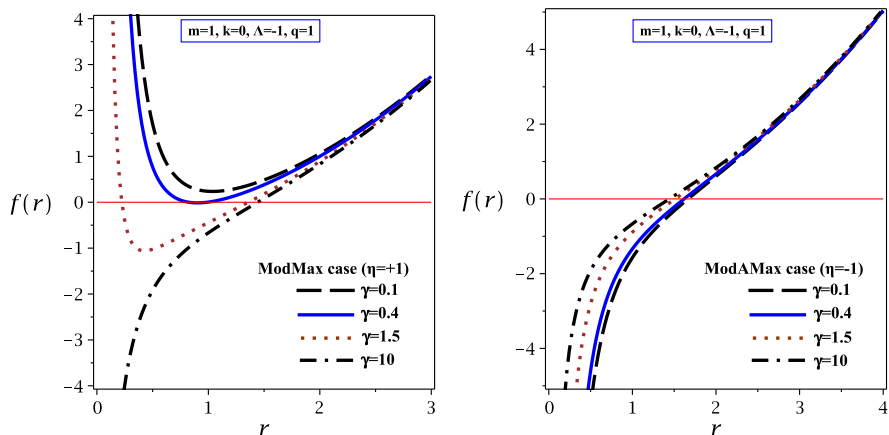
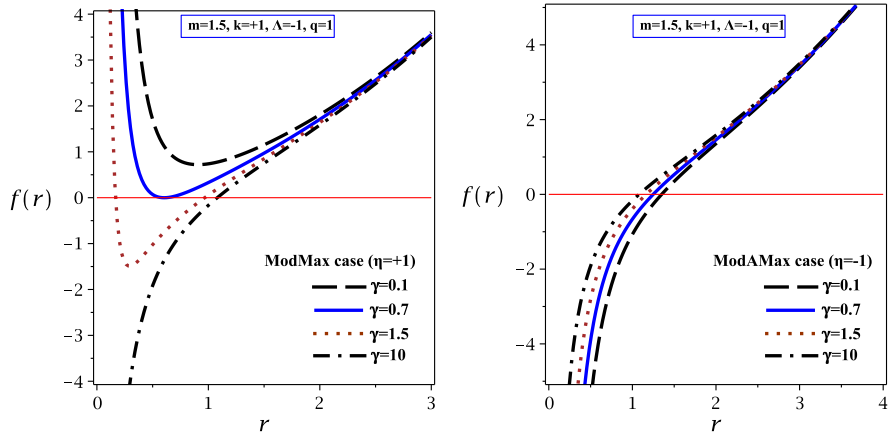
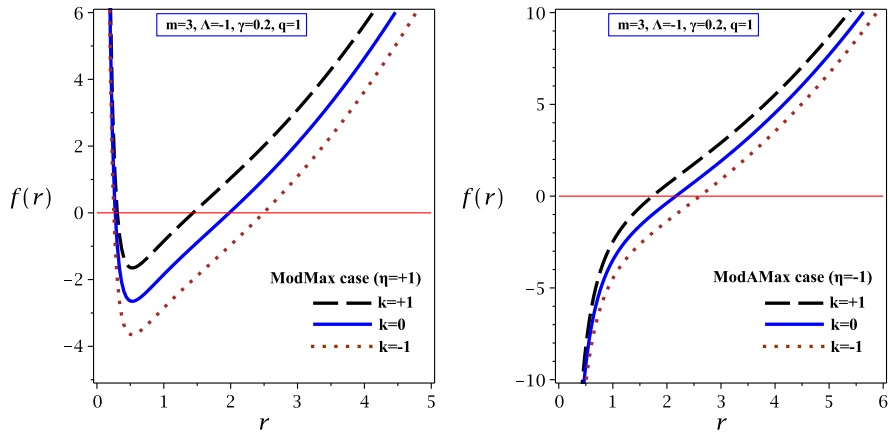
**ModAMax field ( $\eta = -1$ ):** The metric function displays a single root related to the event horizon (see the right panels in Figs. 1 to 4). Results in the right panel of Fig. 1 indicate that the largest and smallest event horizons in the ModAMax scenario correspond to  $k = -1$  and  $k = +1$ , respectively, similar to the ModMax case. Additionally, the event horizon of ModAMax black holes decreases as  $\gamma$  increases (see the right panels in Figs. 2 to 4).

Our analysis reveals two distinct behaviors between ModMax and ModAMax AdS black holes:

- 1) ModMax AdS black holes can have two roots, with the larger root corresponding to the event horizon. In contrast, ModAMax AdS black holes possess only one root, which is associated with the event horizon.
- 2) Increasing the parameter  $\gamma$  results in an increase in the event horizon of ModMax AdS black holes. Conversely, for ModAMax AdS black holes, the event horizon decreases as  $\gamma$  increases.

### III. CONSERVED AND THERMODYNAMIC QUANTITIES: THE FIRST LAW OF THERMODYNAMICS

To investigate the thermodynamic properties of these black holes, we first calculate their Hawking temperature. This requires expressing the geometrical mass  $m$  in terms of the event horizon radius  $r_+$ , the cosmological constant  $\Lambda$ , the electrical charge  $q$ , the ModMax parameter  $\gamma$ , the phantom parameter  $\eta$  (which includes the Maxwell and anti-Maxwell parameters), and the topological constant  $k$ . By considering the metric function



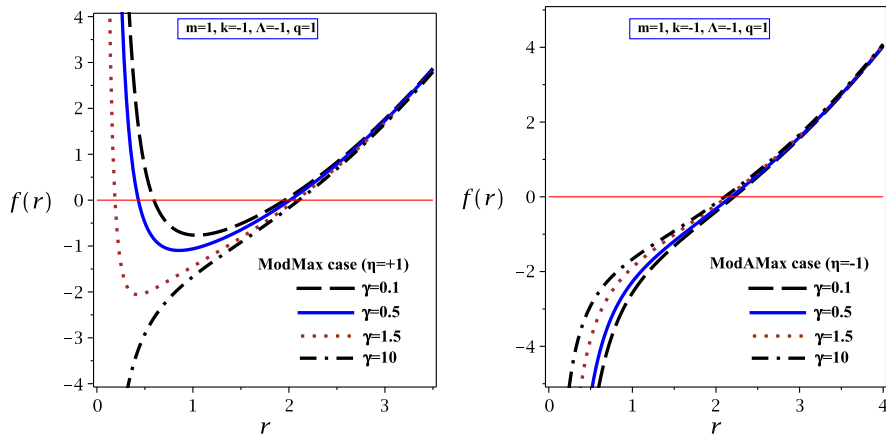


FIG. 4: The metric function  $f(r)$  versus  $r$  for  $k = -1$ , and different values of the ModMax's parameters. Left panel for ModMax case ( $\eta = +1$ ). Right panel for ModAMax or phantom case ( $\eta = -1$ ).

given in Eq. (16), we solve the equation  $f(r) = 0$  to determine the geometrical mass  $m$ , which leads to the following expression

$$m = kr_+ - \frac{\Lambda r_+^3}{3} + \frac{\eta q^2 e^{-\gamma}}{r_+} = \begin{cases} kr_+ - \frac{\Lambda r_+^3}{3} + \frac{q^2 e^{-\gamma}}{r_+}, & \text{ModMax} \\ kr_+ - \frac{\Lambda r_+^3}{3} - \frac{q^2 e^{-\gamma}}{r_+}, & \text{ModAMax} \end{cases} . \quad (21)$$

The Hawking temperature is defined as

$$T = \frac{\kappa}{2\pi}, \quad (22)$$

where  $\kappa$  is related to the surface gravity by

$$\kappa = \sqrt{\frac{-1}{2} (\nabla_\mu \chi_\nu) (\nabla^\mu \chi^\nu)}. \quad (23)$$

By using the metric (9), the Killing vector  $\chi = \partial_t$ , and Eq. (23), we can extract the surface gravity which leads to

$$\kappa = \frac{1}{2} \left. \frac{\partial f(r)}{\partial r} \right|_{r=r_+}, \quad (24)$$

so, by applying Eqs. (21)-(24), we can get the Hawking temperature in the following form

$$T = \frac{1}{4\pi} \left( \frac{k}{r_+} - \Lambda r_+ - \frac{\eta q^2 e^{-\gamma}}{r_+^3} \right) = \begin{cases} \frac{1}{4\pi} \left( \frac{k}{r_+} - \Lambda r_+ - \frac{q^2 e^{-\gamma}}{r_+^3} \right), & \text{ModMax} \\ \frac{1}{4\pi} \left( \frac{k}{r_+} - \Lambda r_+ + \frac{q^2 e^{-\gamma}}{r_+^3} \right), & \text{ModAMax} \end{cases}, \quad (25)$$

where it depends on the  $\Lambda$ ,  $q$ ,  $\gamma$ ,  $\eta$ , and  $k$ .

For the Hawking temperature to be positive ( $T > 0$ ), the system must obey the following condition

$$kr_+^2 - \Lambda r_+^4 - \eta q^2 e^{-\gamma} > 0, \quad (26)$$

in the case of Mod(A)Max AdS black holes, the analysis gives rise to the following two conditions

$$\begin{cases} kr_+^2 - \Lambda r_+^4 - q^2 e^{-\gamma} > 0, & \text{ModMax} \\ kr_+^2 - \Lambda r_+^4 + q^2 e^{-\gamma} > 0, & \text{ModAMax} \end{cases}, \quad (27)$$

and for different values of the topological constant, the above conditions in the ModMax case become

$$T_{\text{ModMax}} > 0 \implies \begin{cases} r_+^2 - \Lambda r_+^4 - q^2 e^{-\gamma} > 0 & k = +1 \\ -\Lambda r_+^4 - q^2 e^{-\gamma} > 0 & k = 0 \\ -r_+^2 - \Lambda r_+^4 - q^2 e^{-\gamma} > 0 & k = -1 \end{cases}, \quad (28)$$

in which  $T_{\text{ModMax}}$  represents the Hawking temperature associated with ModMax black holes. Since the cosmological constant is negative ( $\Lambda < 0$ ) for AdS spacetimes, the Hawking temperature of ModMax AdS black holes is determined by the topological constant ( $k$ ), the electric charge ( $q$ ), and the ModMax parameter ( $\gamma$ ). The interplay among these parameters results in three qualitatively different thermal behaviors:

i) For  $k = +1$ ,  $T_{\text{ModMax}}$  is positive when  $r_+^2 (1 - \Lambda r_+^2) > q^2 e^{-\gamma}$ . It is notable that for the large value of  $\gamma$  (or  $q = 0$ ),  $T_{\text{ModMax}}$  is always positive (see dotted-dashed line in the left panel of Fig. 5).

ii) For the case where  $k = 0$ , the Hawking temperature of ModMax AdS black holes remains positive under the condition  $-\Lambda r_+^4 > q^2 e^{-\gamma}$ . Furthermore,  $T_{\text{ModMax}}$  is always positive when  $q = 0$  (or as  $\gamma \rightarrow$  very large values); this is illustrated by the dotted-dashed lines in the middle panel of Figure. 5.

iii) For the case  $k = -1$ , maintaining a positive Hawking temperature ( $T_{\text{ModMax}} > 0$ ) requires the condition  $-\Lambda r_+^2 > 1 + \frac{3q^2 e^{-\gamma}}{r_+^2}$ .

We present Fig. 5 to further examine the effects of the ModMax parameter and the topological constant on the temperature of ModMax AdS black holes. Our findings are as follows:

1) The left panel of Fig. 5: For  $k = +1$ , there is a critical value for the ModMax parameter, denoted as  $\gamma_{\text{critical}}$ . When  $\gamma > \gamma_{\text{critical}}$ , the temperature of ModMax AdS black holes remains positive, as illustrated by the dashed-dotted line in the left panel of Fig. 5. Conversely, for  $\gamma < \gamma_{\text{critical}}$ , there exists one root for the temperature in the following form

$$r_{+T=0} = \sqrt{\frac{-1 + \sqrt{1 - 4\Lambda q^2 e^{-\gamma}}}{-2\Lambda}}, \quad (29)$$

which the temperature is negative when  $r_+ < r_{+T=0}$  and positive when  $r_+ > r_{+T=0}$ , as shown by the dotted, continuous, and dashed lines in the left panel of Fig. 5. This indicates that large ModMax AdS black holes possess positive temperatures, while small ModMax AdS black holes have negative temperatures. Additionally, as the value of  $\gamma$  increases, the range of positive temperatures also expands.

2) Middle panel in Fig. 5: For  $k = 0$ , there is one real root that depends on the cosmological constant, the electric charge, and the ModMax parameter, expressed as follows

$$r_{+T=0} = \sqrt{\frac{\sqrt{-4\Lambda q^2 e^{-\gamma}}}{-2\Lambda}}, \quad (30)$$

where the root decreases as  $\gamma$  increases and  $q$  decreases. The Hawking temperature is negative for  $r_+ < r_{+T=0}$  (i.e., in this range,  $T$  is negative), while for  $r_+ > r_{+T=0}$ , the temperature of ModMax AdS black holes becomes positive (see the middle panel in Fig. 5). This indicates that small ModMax AdS black holes exhibit negative temperatures, whereas larger ones have positive temperatures. According to Eq. (30), the range of positive temperatures increases as  $\gamma$  increases or  $q$  decreases. In essence, the electric charge counteracts the effects of the ModMax parameter. Notably, no real root exists when  $\gamma$  takes on very large values or when  $q = 0$  (indicated by the dotted-dashed line in the middle panel of Figure. 5). An interesting effect of the ModMax parameter on the Hawking temperature of these black holes is observed: for very large values of  $\gamma$  (or in the absence of  $q$ ), the Hawking temperature vanishes as  $r_+ \rightarrow 0$  (i.e.,  $\lim_{r_+ \rightarrow 0} T \rightarrow 0$ ).

3) Right panel in Fig. 5: For  $k = -1$ , there is one real root, which exists in the following form

$$r_{+T=0} = \sqrt{\frac{1 + \sqrt{1 - 4\Lambda q^2 e^{-\gamma}}}{-2\Lambda}}, \quad (31)$$

and it depends on  $\Lambda$ ,  $q$ , and  $\gamma$ . The real root decreases as  $\gamma$  increases (or as  $q$  decreases). The temperature is negative when  $r_+ < r_{+T=0}$  and positive when  $r_+ > r_{+T=0}$ . Thus, the temperatures of the small and large ModMax AdS black holes are negative and positive, respectively.

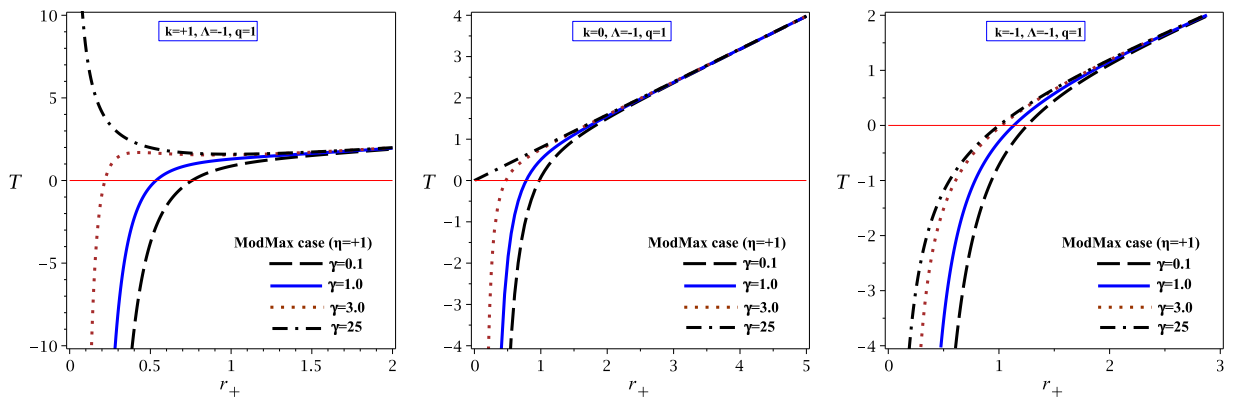


FIG. 5: The Hawking temperature  $T$  versus  $r_+$  for  $k = +1$  (left panel),  $k = 0$  (middle panel), and  $k = -1$  (right panel) by considering the ModMax field ( $\eta = +1$ ).

For the Hawking temperature of ModAMax AdS black holes to be positive, we find that

$$T_{\text{ModAMax}} > 0 \implies \begin{cases} r_+^2 - \Lambda r_+^4 + q^2 e^{-\gamma} > 0 & k = +1 \\ -\Lambda r_+^4 + q^2 e^{-\gamma} > 0 & k = 0 \\ -r_+^2 - \Lambda r_+^4 + q^2 e^{-\gamma} > 0 & k = -1 \end{cases}, \quad (32)$$

where  $T_{\text{ModAMax}}$  denotes the Hawking temperature of ModAMax black holes. The Hawking temperature of ModAMax AdS black holes is a function of  $k$ ,  $q$ , and  $\gamma$ , leading to three distinct thermodynamic behaviors:

- i) For  $k = +1$ :  $T_{\text{ModAMax}}$  is always positive (as shown in the left panel of Figure. 6).
- ii) For  $k = 0$ : Similar to the  $k = +1$  case, the Hawking temperature of ModAMax AdS black holes is consistently positive (see the middle panel of Figure. 6).
- iii) For  $k = -1$ : To ensure a positive Hawking temperature ( $T_{\text{ModAMax}} > 0$ ), the following condition must be met:  $-\Lambda r_+^2 + \frac{q^2 e^{-\gamma}}{r_+^2} > 1$ . This condition explicitly reveals that the Hawking temperature of ModAMax AdS black holes can become negative when  $k = -1$  (illustrated in the right panel of Figure. 6).

We plot Fig. 6 to further examine the effects of the ModMax parameter and the topological constant on the temperature of ModAMax AdS black holes. Our results are as follows:

- 1) The left panel in Fig. 6 shows that for  $k = +1$ , the Hawking temperature of ModAMax AdS black holes is consistently positive. Varying the ModMax parameter has a minimal effect on the temperature of small black holes.
- 2) The middle panel in Fig. 6 illustrates that for  $k = 0$ , no roots exist. As the radius decreases, the Hawking temperature initially decreases and reaches a minimum value that depends on  $\gamma$ . Beyond this point, the temperature rises sharply. Moreover, for very large values of  $\gamma$  (or when  $q = 0$ ), the temperature approaches zero as  $r_+ \rightarrow 0$  (i.e.,  $\lim_{r_+ \rightarrow 0} T \rightarrow 0$ ).
- 3) The right panel in Fig. 6 shows that for  $k = -1$ , there is one root for the temperature, expressed in the following form

$$r_{+T=0} = \sqrt{\frac{2 + 2\sqrt{1 + 4\Lambda q^2 e^{-\gamma}}}{-\Lambda}}, \quad (33)$$

provided  $q^2 e^{-\gamma} > \frac{-1}{4\Lambda}$ . This root increases as  $\gamma$  decreases (or  $q$  increases). The temperature is negative for  $r_+ < r_{+T=0}$  and positive for  $r_+ > r_{+T=0}$ . Consequently, the temperature of the small ModAMax AdS black hole can attain both negative and positive values, a behavior dependent on  $\gamma$ .

Using Gauss's law, we can express the electric charge of a black hole per unit volume ( $\mathcal{V}$ ) in the following way

$$Q = \frac{\tilde{Q}}{\mathcal{V}} = \frac{F_{tr}}{4\pi} \int_0^{2\pi} \int_0^\pi \sqrt{g_k} d\theta d\varphi = \frac{q}{4\pi}. \quad (34)$$

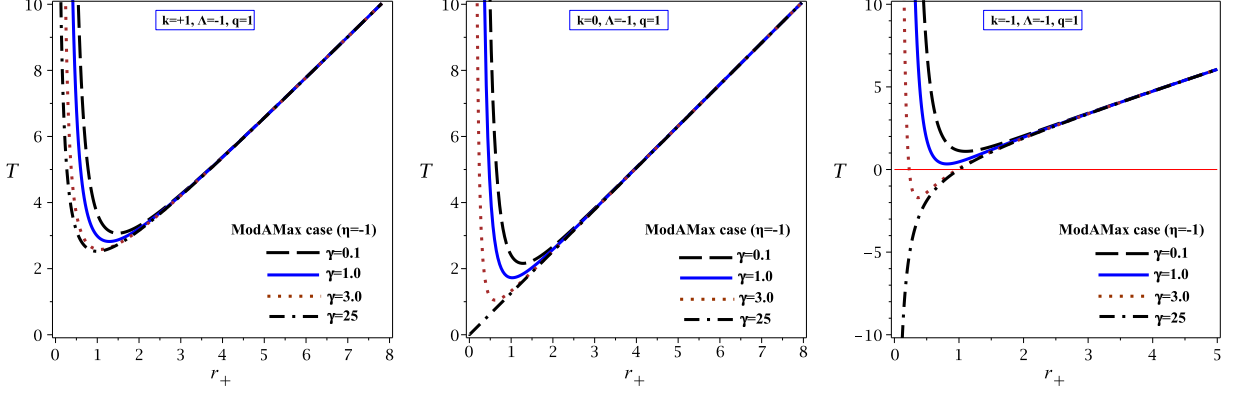


FIG. 6: The Hawking temperature  $T$  versus  $r_+$  for  $k = +1$  (left panel),  $k = 0$  (middle panel), and  $k = -1$  (right panel) by considering the ModAMax field ( $\eta = -1$ ).

where  $F_{tr} = \frac{q}{r^2}$ , and for case  $t = \text{constant}$  and  $r = \text{constant}$ , the determinant of metric tensor  $g_k$  is  $r^4 \det(d\Omega_k^2)$  (i.e.,  $g_k = \det(g_k) = r^4 \det(d\Omega_k^2)$ ). Furthermore,  $\mathcal{V} = \int_0^{2\pi} \int_0^\pi \sqrt{\det(d\Omega_k^2)} d\theta d\varphi$ , where  $\mathcal{V}$  is the area of a unit volume of constant  $(t, r)$  space. For example,  $\mathcal{V}$  is  $4\pi$  for  $k = 1$ .

The electric potential at the event horizon ( $U$ ), relative to the reference point at infinity ( $r \rightarrow \infty$ ), is given by

$$U = A_\mu \chi^\mu |_{r \rightarrow \infty} - A_\mu \chi^\mu |_{r \rightarrow r_+} = \frac{qe^{-\gamma}}{r_+}, \quad (35)$$

where the gauge potential is zero when  $r \rightarrow \infty$ .

Applying the area law, we can get the entropy of the topological Mod(A)Max black holes per unit volume ( $\mathcal{V}$ ), which leads to

$$S = \frac{\tilde{S}}{\mathcal{V}} = \frac{\mathcal{A}}{4\mathcal{V}} = \frac{\int_0^{2\pi} \int_0^\pi \sqrt{g_{\theta\theta} g_{\varphi\varphi}} |_{r=r_+}}{4} = \frac{r_+^2}{4}, \quad (36)$$

where  $\mathcal{A}$  is the horizon area.

The Ashtekar-Magnon-Das (AMD) approach [124, 125] for four-dimensional spacetime is

$$\widetilde{M} = \frac{-\ell}{8\pi} \oint_S \hat{E}_t^t dS, \quad (37)$$

where  $\ell^2 = -3/\Lambda$  is AdS radius. Generally, the quantity  $\hat{E}_\nu^\mu = \Omega^{-1} C_{\rho\nu\sigma}^\mu n^\rho n^\sigma$  is defined as the electric part of the Weyl tensor with respect to the unit normal  $n^\rho$  at conformal infinity. Here,  $\Omega$  is the conformal factor bringing the AdS boundary to a finite coordinate location ( $\Omega = \frac{1}{r}$  for AdS). Also,  $C_{\rho\nu\sigma}^\mu$  denotes the Weyl tensor. Then,  $\hat{E}_t^t = \Omega^{-1} C_{\rho t\sigma}^t n^\rho n^\sigma$ , which, for the given spacetime (9), reduces to  $\hat{E}_t^t = \Omega^{-1} C_{rtr}^t n^r n^r \propto \Omega^{-1} C_{rtr}^t$ . Now, the Weyl tensor component  $C_{rtr}^t$  for these black holes is found to be

$$C_{rtr}^t \sim \frac{-m}{r^3} + \frac{\eta q^2 e^{-\gamma}}{r^4} + O\left(\frac{1}{r^5}\right), \quad (38)$$

so that  $\hat{E}_t^t$  takes the following asymptotic form

$$\hat{E}_t^t = \frac{-m}{r^2} + \frac{\eta q^2 e^{-\gamma}}{r^3}. \quad (39)$$

Substituting Eqs. (38), (39), and  $dS = r^2 d\Omega_k^2$  into the AMD intergral (37), we obtain

$$\widetilde{M} = \frac{-\ell}{8\pi} \lim_{r \rightarrow \infty} \oint_S \left( \frac{-m}{r^2} + O\left(\frac{1}{r^3}\right) \right) dS = \frac{-\ell}{8\pi} (r^2 \mathcal{V}) \left( \frac{-m}{r^2} \right) = \frac{m\mathcal{V}}{8\pi}. \quad (40)$$

Hence, the total mass of the topological Mod(A)Max black holes per unit volume  $\mathcal{V}$ , is given by

$$M = \frac{\widetilde{M}}{\mathcal{V}} = \frac{m}{8\pi} = \frac{1}{8\pi} \left( kr_+ - \frac{\Lambda r_+^3}{3} + \frac{\eta q^2 e^{-\gamma}}{r_+} \right) = \begin{cases} \frac{1}{8\pi} \left( kr_+ - \frac{\Lambda r_+^3}{3} + \frac{q^2 e^{-\gamma}}{r_+} \right), & \text{ModMax} \\ \frac{1}{8\pi} \left( kr_+ - \frac{\Lambda r_+^3}{3} - \frac{q^2 e^{-\gamma}}{r_+} \right), & \text{ModAMax} \end{cases}, \quad (41)$$

in the above equation, we use from the geometrical mass (21).

To ensure that the total mass remains positive, the following constraint must be satisfied

$$M > 0 \implies 3kr_+^2 - \Lambda r_+^4 + 3\eta q^2 e^{-\gamma} > 0, \quad (42)$$

where, for Mod(A)Max AdS black holes, this leads to the following two conditions

$$\begin{cases} 3kr_+^2 - \Lambda r_+^4 + 3q^2 e^{-\gamma} > 0, & \text{ModMax} \\ 3kr_+^2 - \Lambda r_+^4 - 3q^2 e^{-\gamma} > 0, & \text{ModAMax} \end{cases}. \quad (43)$$

Moreover, for different values of the topological constant, the above conditions in the ModMax case reduce to

$$M_{\text{ModMax}} > 0 \implies \begin{cases} 3r_+^2 - \Lambda r_+^4 + 3q^2 e^{-\gamma} > 0 & k = +1 \\ -\Lambda r_+^4 + 3q^2 e^{-\gamma} > 0 & k = 0 \\ -3r_+^2 - \Lambda r_+^4 + 3q^2 e^{-\gamma} > 0 & k = -1 \end{cases}, \quad (44)$$

where  $M_{\text{ModMax}}$  denotes the total mass of ModMax black holes. On the other hand, since the cosmological constant is negative ( $\Lambda < 0$ ) for AdS black holes, the total mass of ModMax AdS black holes depends on the topological constant ( $k$ ), the electric charge ( $q$ ), and the ModMax parameter ( $\gamma$ ), leading to three distinct behaviors:

i) For the case  $k = +1$  (where  $3r_+^2 - \Lambda r_+^4 + 3q^2 e^{-\gamma} > 0$ ),  $M_{\text{ModMax}}$  is always positive across all radii (as shown by the thick lines in the left panel of Fig. 7). Notably,  $\lim_{r_+ \rightarrow 0} M_{\text{ModMax}} \rightarrow 0$  when  $q = 0$  (or equivalently, when  $\gamma \rightarrow$  very large value), which is illustrated by the thick, dotted-dashed line in the left panel of Fig. 7.

ii) For the case  $k = 0$  (under the condition  $-\Lambda r_+^4 + 3q^2 e^{-\gamma} > 0$ ), similar to the preceding case,  $M_{\text{ModMax}}$  is consistently positive across all radii (as shown by the thick lines in the middle panel of Fig. 7). Notably, the total mass of ModMax AdS black holes is zero at  $r_+ = 0$ , meaning  $\lim_{r_+ \rightarrow 0} M_{\text{ModMax}} \rightarrow 0$  when  $q = 0$  (or when  $\gamma \rightarrow$  very large value), which is illustrated by the thick, dotted-dashed line in the middle panel of Fig. 7.

iii) For the case  $k = -1$ , ensuring a positive value for  $M_{\text{ModMax}}$  requires the satisfaction of the condition  $\frac{-\Lambda r_+^2}{3} + \frac{q^2 e^{-\gamma}}{r_+^2} > 1$ . This condition implies that the total mass of ModMax AdS black holes cannot be positive at any radius (as demonstrated by the thick lines in the right panel of Fig. 7).

To ensure that the total mass of ModAMax AdS black holes is positive, we find that

$$M_{\text{ModAMax}} > 0 \implies \begin{cases} 3r_+^2 - \Lambda r_+^4 - 3q^2 e^{-\gamma} > 0 & k = +1 \\ -\Lambda r_+^4 - 3q^2 e^{-\gamma} > 0 & k = 0 \\ -3r_+^2 - \Lambda r_+^4 - 3q^2 e^{-\gamma} > 0 & k = -1 \end{cases}, \quad (45)$$

where  $M_{\text{ModAMax}}$  represents the total mass of ModAMax black holes. The total mass of ModAMax AdS black holes is determined by the topological constant  $k$ , the electric charge  $q$ , and the ModAMax parameter  $\gamma$ ; these dependencies give rise to three distinct physical behaviors:

i) For  $k = +1$ ,  $M_{\text{ModAMax}}$  remains positive when  $r_+^2 (3 - \Lambda r_+^2) > 3q^2 e^{-\gamma}$ . This condition indicates that the total mass of ModAMax AdS black holes cannot be positive at any radius (see the thick lines in the left panel of Fig. 8). Furthermore, in the limit  $r_+ \rightarrow 0$ ,  $M_{\text{ModAMax}} \rightarrow 0$  when  $q = 0$  (or when  $\gamma$  approaches a very large value), see the thick dotted-dashed lines in the left panel of Fig. 8.

ii) For  $k = 0$ ,  $M_{\text{ModAMax}}$  becomes positive under the condition  $-\Lambda r_+^4 > 3q^2 e^{-\gamma}$ . Moreover, as  $r_+ \rightarrow 0$ , the total mass tends to zero for  $q = 0$  or when  $\gamma$  approaches very large values, consistent with the thick dotted-dashed lines in the middle panel of Fig. 8.

iii) To ensure a positive value of  $M_{\text{ModAMax}}$  for  $k = -1$ , the condition  $\frac{-\Lambda r_+^2}{3} > 1 + \frac{q^2 e^{-\gamma}}{r_+^2}$  must be satisfied. Moreover, in the absence of electric charge, the total mass of ModAMax AdS black holes becomes positive when  $-\Lambda r_+^2 > 3$  (see the thick lines in the right panel of Fig. 8).

We study the high energy limit and the asymptotic limit of the total mass to evaluate the effects of various parameters. The high energy limit of the total mass is given by

$$\lim_{r_+ \rightarrow 0} M \propto \frac{\eta q^2 e^{-\gamma}}{r_+} = \begin{cases} \frac{q^2 e^{-\gamma}}{8\pi r_+}, & \text{ModMax} \\ -\frac{q^2 e^{-\gamma}}{8\pi r_+}, & \text{ModAMax} \end{cases}, \quad (46)$$

where for small black holes, the total mass is determined solely by the electrodynamic field. It is evident that the mass of small ModMax AdS black holes can be positive. In contrast, the total mass of small ModAMax black holes cannot be positive. This is the main difference between ModMax and ModAMax fields in the high energy limit of the total mass of black holes.

The asymptotic limit of the total mass depends solely on the cosmological constant, expressed as

$$\lim_{r_+ \rightarrow \infty} M \propto -\frac{\Lambda r_+^3}{24\pi}, \quad (47)$$

where indicates that the total mass of the large Mod(A)Max AdS black hole is always positive.

The term  $\frac{kr_+}{8\pi}$  in Eq. (41) is significant for medium black holes. Specifically, the total mass of medium ModMax AdS black holes can be negative when  $k = -1$ . Additionally, in the high energy limit (or for small black holes), the total mass, as shown in Eq. (46), is influenced by the electrodynamic field and is expressed as  $\frac{\eta q^2 e^{-\gamma}}{8\pi r_+}$ . This mass increases as  $r_+$  approaches 0, implying that small black holes may possess an implausibly large mass. To identify an appropriate range for the total mass, we present the total mass and temperature together in Figs. 7 and 8.

In Fig. 7, we examine the simultaneous effects of the ModMax parameter and the topological constant on total mass (thick lines) and temperature (thin lines). Our analysis indicates that:

1) In the left panel of Fig. 7, for  $k = +1$ , increasing  $r_+$  initially causes the total mass,  $M$ , to decrease until it reaches a critical point where the slope of  $M$  is zero (i.e.,  $\frac{dM}{dr_+} = 0$ ). Beyond this point,  $M$  begins to increase as  $r_+$  continues to rise. This critical point corresponds to the zero point of the temperature, as indicated by the relation  $T = \frac{dM}{dr_+} / \frac{dS}{dr_+}$ . Specifically, there exists a critical radius for the total mass, denoted as  $r_{+T=0}$ . For values of  $r_+ < r_{+T=0}$ , black holes cannot be defined because the temperature in this region is negative, rendering the thermodynamic system non-physical. Conversely, for  $r_+ > r_{+T=0}$ , the temperature becomes positive, and the total mass increases with  $r_+$ . This indicates that the mini ModMax AdS black holes (i.e., those with  $r_+ < r_{+T=0}$ ) cannot be considered physical objects (refer to the dashed, continuous, and dotted thin lines in the left panel of Fig. 7). Additionally, as  $\gamma$  increases, the critical point for total mass can be eliminated, allowing small ModMax AdS black holes to be considered physical objects. In fact, for sufficiently large values of  $\gamma$ , the critical point disappears entirely, permitting black holes of any radius to exist (see the dotted-dashed line in the left panel of Fig. 7). Thus, the ModMax parameter significantly influences the physical area of black holes, highlighting that the physical area of ModMax AdS black holes expands with increasing  $\gamma$ .

2) In the middle panel of Fig. 7, for  $k = 0$ , the total mass behaves similarly to the previous case with  $k = +1$ . However, when comparing the left and middle panels, there are two notable differences between  $k = 0$  and  $k = +1$ : i) For large values of  $\gamma$ , very small ModMax AdS black holes cannot be considered physical objects for  $k = 0$ , as their temperature becomes negative while the total mass approaches zero (see the dashed-dotted line in the middle panel of Fig. 7). In contrast, ModMax AdS black holes are physical objects at any radius for  $k = +1$  (see the dashed-dotted line in the left panel of Fig. 7). ii) The physical area for  $k = +1$  is larger than that for  $k = 0$ .

3) In the right panel of Fig. 7, for  $k = -1$ , there exists a critical value for the ModMax parameter ( $\gamma_{\text{critical}}$ ). When  $\gamma > \gamma_{\text{critical}}$ , the total mass of ModMax black holes with  $r_+ > r_{+T=0}$  becomes negative, even though the temperature remains positive. Conversely, when  $\gamma < \gamma_{\text{critical}}$ , the total mass of these black holes is positive in the same region ( $r_+ > r_{+T=0}$ ), as indicated by the dashed line in the right panel of Fig. 7. Additionally, the physical area decreases as  $\gamma$  increases.

By comparing the behavior of the total mass and the Hawking temperature, we observe two notable results:

i) For ModMax AdS black holes with  $k = +1$ , the physical area (defined as the area where both  $M > 0$  and  $T > 0$ ) is superior to that of other topological cases.

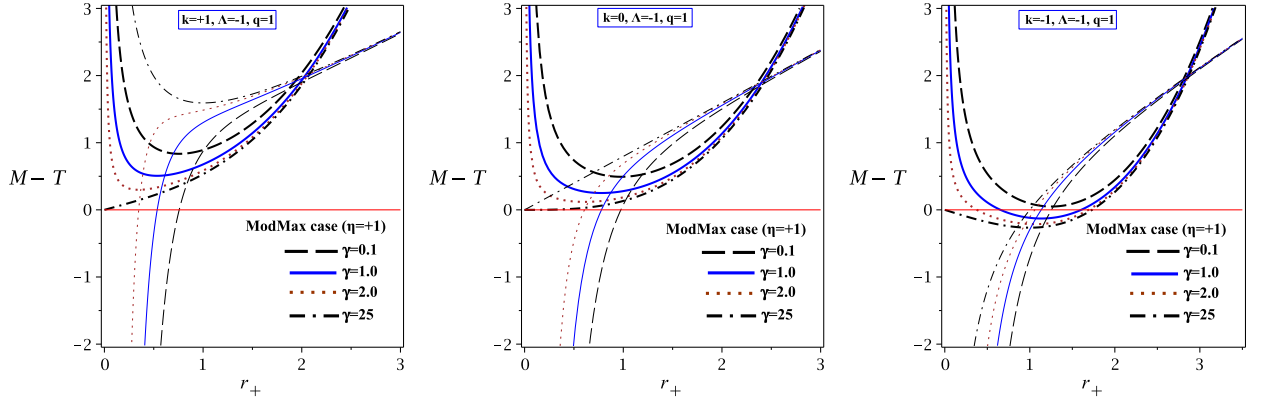


FIG. 7: The total mass  $M$  (thick lines) and the Hawking temperature  $T$  (thin lines) versus  $r_+$  for  $k = +1$  (left panel),  $k = 0$  (middle panel), and  $k = -1$  (right panel) by considering the ModMax field ( $\eta = +1$ ).

ii) As  $\gamma$  increases, the physical area increases for both  $k = +1$  and  $k = 0$ ; however, for  $k = -1$ , the physical area decreases with an increase in  $\gamma$ .

In Fig. 8, we examine the effects of the ModMax parameter and topological constant by analyzing the impact of a phantom field on both total mass (thick lines) and temperature (thin lines) simultaneously. Our findings reveal that:

1) In the left panel of Fig. 8, for  $k = +1$ , we observe that the total mass of the ModAMax AdS black hole is negative before a certain root and becomes positive thereafter, consistent with our expectations from Eq. (46). Furthermore, as  $\gamma$  increases, the region of negative mass decreases, and for sufficiently large values of  $\gamma$ , the negative mass region is eliminated (as indicated by the dashed-dotted line in the left panel of Fig. 8). Additionally, the temperature of ModAMax black holes remains positive at all radii, which means that increasing  $\gamma$  leads to an increase in the physical area.

2) In the middle panel of Fig. 8, for  $k = 0$ , the behavior of the mass of small black holes resembles that of the previous case ( $k = +1$ ). Specifically, there is a root, and the small black holes cannot meet the positive mass condition. Additionally, as the value of  $\gamma$  increases, the negative area of the mass decreases. However, for very large values of the ModMax parameter, the negative area of the total mass can be eliminated (as shown by the dashed-dotted line in the left panel of Fig. 8). Similar to the previous case, the temperature of these black holes remains positive throughout, resulting in an increase in the physical area as  $\gamma$  increases.

3) In the right panel of Fig. 8, for  $k = -1$ , the large ModAMax black holes satisfy the physical conditions, as both mass and temperature are positive. Additionally, the physical area of these large black holes increases with increasing  $\gamma$ . In contrast, for small ModAMax black holes, both temperature and mass are negative for every value of  $\gamma$ . Therefore, small ModAMax AdS black holes cannot be considered physical objects.

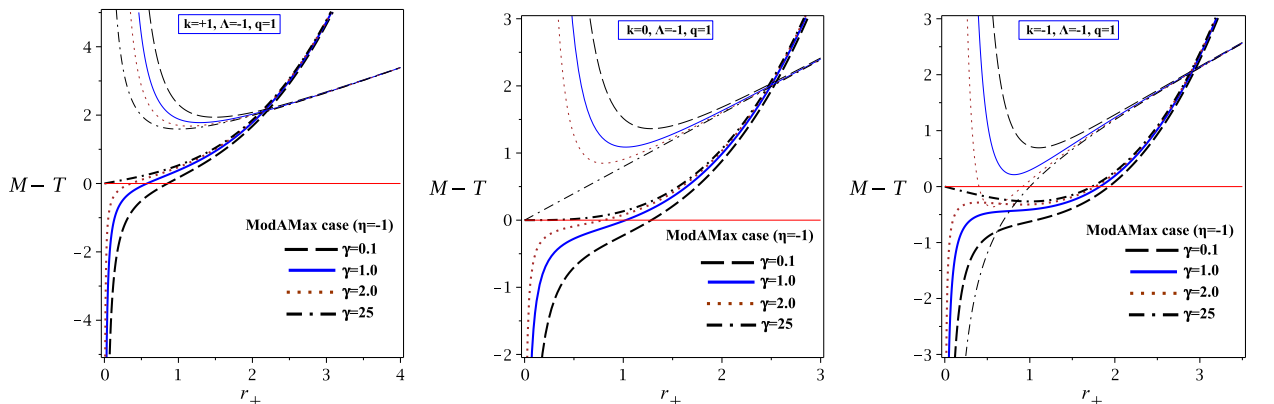


FIG. 8: The total mass  $M$  (thick lines) and the Hawking temperature  $T$  (thin lines) versus  $r_+$  for  $k = +1$  (left panel),  $k = 0$  (middle panel), and  $k = -1$  (right panel) by considering the ModAMax field ( $\eta = -1$ ).

We can now state that the conserved and thermodynamic quantities obtained in Eqs. (25), (34), (35), (36), and (41) satisfy the first law of thermodynamics in the following form

$$dM = TdS + \eta UdQ = \begin{cases} TdS + UdQ & \text{ModMax} \\ TdS - UdQ & \text{ModAMax} \end{cases}, \quad (48)$$

where  $T = \left(\frac{\partial M}{\partial S}\right)_Q$ , and  $U = \left(\frac{\partial M}{\partial Q}\right)_S$  are, respectively, in agreement with those calculated in Eqs. (25) and (35).

#### IV. LOCAL AND GLOBAL STABILITIES

This section is dedicated to the investigation of the local and global stabilities of the topological Mod(A)Max AdS black holes, utilizing the thermodynamic variables of heat capacity, as well as the Helmholtz and Gibbs free energies. Specifically, we analyze the influence of both the topological constant ( $k$ ) and the ModMax parameter ( $\gamma$ ) on these stability criteria.

##### A. Local Stability

In the framework of the canonical ensemble, the local stability of a thermodynamical system can be analyzed through its heat capacity. The heat capacity encodes essential information about the thermal structure of black holes and provides three particularly significant insights, which are; i) Discontinuities in the heat capacity indicate possible thermal phase transitions that the system may experience. ii) The sign of the heat capacity determines the thermal stability of the system; a positive value corresponds to stability, whereas a negative one signifies instability. iii) The zeros (roots) of the heat capacity are also of interest, as they may signal transitions between stable and unstable phases or represent boundary points. Motivated by these considerations, we calculate the heat capacity of the obtained solutions and analyze the local thermodynamic stability of the corresponding black holes based on this quantity.

Prior to calculating the heat capacity, we first rewrite the expression for the total mass of the black hole (41) in terms of the electric charge (Eq. (34)), and the entropy (Eq. (36)) in the following form

$$M(S, Q) = \frac{3kS - 4\Lambda S^2 + 12\eta\pi^2 Q^2 e^{-\gamma}}{12\pi\sqrt{S}}, \quad (49)$$

using Equation (49), the temperature is rewritten in the following form

$$T = \left(\frac{\partial M(S, Q)}{\partial S}\right)_Q = \frac{kS - 4\Lambda S^2 - 4\eta\pi^2 Q^2 e^{-\gamma}}{8\pi S^{3/2}}, \quad (50)$$

The heat capacity is defined by the relation

$$C_Q = \frac{T}{\left(\frac{\partial T}{\partial S}\right)_Q} = \frac{\left(\frac{\partial M(S, Q)}{\partial S}\right)_Q}{\left(\frac{\partial^2 M(S, Q)}{\partial S^2}\right)_Q}, \quad (51)$$

by considering Eqs. (49) and (50) within Eq. (51), the resulting expression for the heat capacity is

$$C_Q = \frac{2(4\Lambda S^2 - kS + 4\eta\pi^2 Q^2 e^{-\gamma})S}{kS + 4\Lambda S^2 - 12\eta\pi^2 Q^2 e^{-\gamma}}. \quad (52)$$

Within the context of black hole thermodynamics, the roots of the heat capacity, where  $C_Q = 0$  (or  $T = 0$ ), are generally considered to represent the boundary between physically admissible black holes (where temperature  $T > 0$ ) and non-physical solutions (where  $T < 0$ ). We refer to these points as physical limitation points. It is noteworthy that at these specific points, the sign of the heat capacity changes. Furthermore, the divergences (singularities) in the heat capacity are understood to correspond to the critical points of thermal phase transitions for these black holes. Consequently, the critical points for the phase transitions and

the aforementioned limitation points, as determined by the heat capacity analysis, are calculated using the following relations:

$$\begin{cases} T = \left( \frac{\partial M(S, Q)}{\partial S} \right)_Q = 0, & \text{physical limitation points} \\ \left( \frac{\partial^2 M(S, Q)}{\partial S^2} \right)_Q = 0, & \text{phase transition critical points} \end{cases} \quad (53)$$

Now, we obtain physical limitation points by solving (50) in terms of the entropy as

$$\begin{cases} S_{root_1} = \frac{k + \sqrt{k^2 - 64\pi^2\Lambda\eta Q^2 e^{-\gamma}}}{8\Lambda}, \\ S_{root_2} = \frac{k - \sqrt{k^2 - 64\pi^2\Lambda\eta Q^2 e^{-\gamma}}}{8\Lambda}, \end{cases} \quad (54)$$

To have the real root(s), we have to respect  $k^2 \geq 64\pi^2\Lambda\eta Q^2 e^{-\gamma}$ . By considering this constraint and this fact that we consider AdS case ( $\Lambda < 0$ ), we find that there is one real positive root for the heat capacity and it is related to  $S_{root_2}$ . Indeed  $S_{root_1}$  leads to negative value and  $S_{root_2}$  includes a real positive value and determine the physical limitation point of the thermodynamical system. In addition, the physical limitation point ( $S_{root_2}$ ) depends on various parameters such as  $k$ ,  $Q$ ,  $\eta$ ,  $\Lambda$ , and  $\gamma$ . We study the effects of these parameters on the physical limitation point of Mod(A)Max AdS black holes ( $S_{root_2}$ ), and we find that

**ModMax field ( $\eta = +1$ ):** Considering  $\eta = +1$ , and for different topological constant we find that

$$\text{physical limitation point for ModMax case} \implies \begin{cases} S_{root_2} = \frac{-1 + \sqrt{1 - 64\pi^2\Lambda Q^2 e^{-\gamma}}}{-8\Lambda}, & k = +1 \\ S_{root_2} = \frac{\sqrt{-64\pi^2\Lambda Q^2 e^{-\gamma}}}{-8\Lambda}, & k = 0 \\ S_{root_2} = \frac{1 + \sqrt{1 - 64\pi^2\Lambda Q^2 e^{-\gamma}}}{-8\Lambda}, & k = -1 \end{cases}, \quad (55)$$

which indicates that the largest root belongs to  $k = -1$ , and the smallest root is related to  $k = +1$ . In other words, by fixing other values of parameter (such as  $\Lambda$ ,  $Q$ , and  $\gamma$ ), we find that a order for the physical limitation point which depends on the topological constant as  $S_{root_2|k=+1} < S_{root_2|k=0} < S_{root_2|k=-1}$ . On the other hand, by increasing  $\gamma$  the physical limitation point decreases (see thick dotted-dashed and dashed lines in Fig. 9). Also, for very large values of  $\gamma$ , the physical limitation point disappear for  $k = +1$  and  $k = 0$ , because  $\lim_{\gamma \rightarrow \infty} S_{root_2} \rightarrow 0$ . However, for  $k = -1$ , the physical limitation point goes to  $\frac{-1}{4\Lambda}$  ( $\lim_{\gamma \rightarrow \infty} S_{root_2} \rightarrow \frac{-1}{4\Lambda}$  when  $k = -1$ ).

**ModAMax field ( $\eta = -1$ ):** By replacing  $\eta = -1$  in the root  $S_{root_2}$ , we find that the following coditions for different values of the topological constants

$$\text{physical limitation point for ModAMax case} \implies \begin{cases} S_{root_2} = \frac{1 - \sqrt{1 + 64\pi^2\Lambda Q^2 e^{-\gamma}}}{8\Lambda}, & k = +1 \\ S_{root_2} = \frac{\sqrt{64\pi^2\Lambda Q^2 e^{-\gamma}}}{-8\Lambda}, & k = 0 \\ S_{root_2} = \frac{1 + \sqrt{1 + 64\pi^2\Lambda Q^2 e^{-\gamma}}}{-8\Lambda}, & k = -1 \end{cases}, \quad (56)$$

there is no the real positive physical limitation point for ModAMax AdS black holes for  $k = +1$  and  $k = 0$  (see thick lines in Fig. 10, for more details). However, for  $k = -1$ , one real positive root for the heat capacity exists when  $\gamma \rightarrow$  very large values (see the thick continuous line in the right panel of Fig. 10). Also, similar to the previous case, for  $k = -1$  and in the limit  $\gamma \rightarrow \infty$ ,  $S_{root_2} \rightarrow \frac{-1}{4\Lambda}$ .

In order to study the phase transition critical points (or divergence points of the heat capacity), we have to solve the relation  $\left( \frac{\partial^2 M(S, Q)}{\partial S^2} \right)_Q = 0$ . So, we have

$$\begin{cases} S_{div_1} = \frac{-k + \sqrt{k^2 + 192\pi^2\Lambda\eta Q^2 e^{-\gamma}}}{8\Lambda}, \\ S_{div_2} = \frac{-k - \sqrt{k^2 + 192\pi^2\Lambda\eta Q^2 e^{-\gamma}}}{8\Lambda}, \end{cases}, \quad (57)$$

where indicate that we have to respect  $k^2 \geq -192\pi^2\Lambda\eta Q^2e^{-\gamma}$ , for having the real divergent point(s). Our analysis shows that the heat capacity of these black holes has one divergent point and it related to  $S_{div_2}$ . This divergent point depends on various parameters such as  $k$ ,  $Q$ ,  $\eta$ ,  $\Lambda$ , and  $\gamma$ . Now, we evaluate the effects of these parameters on the phase transition critical point of Mod(A)Max AdS black holes ( $S_{div_2}$ ), and we find that

**ModMax field ( $\eta = +1$ ):** Considering  $\eta = +1$ ,  $\Lambda < 0$ , and different values of topological constant within Eq. (50), we find that there is no real positive divergence point for heat capacity for  $k = 0$ , and  $k = -1$  (see the thick lines in the middel and right panels in Fig. 9). However, for  $k = +1$ , it is possible to find two the phase transition critical points which are

$$\text{phase transition critical points for ModMax} \implies \begin{cases} S_{div_1} = \frac{1-\sqrt{1+192\pi^2\Lambda Q^2e^{-\gamma}}}{-8\Lambda}, & k = +1 \\ S_{div_2} = \frac{1+\sqrt{1+192\pi^2\Lambda Q^2e^{-\gamma}}}{-8\Lambda}, & k = +1 \end{cases}, \quad (58)$$

and  $S_{div_2}$  is located in larger entropy than  $S_{div_1}$  (i.e.,  $S_{div_2} > S_{div_1}$ ). It is notable that in the limit  $\gamma \rightarrow \infty$ , the phase transition critical points reduce from two to one real root, because  $\lim_{\gamma \rightarrow \infty} S_{div_1} \rightarrow 0$ , and  $\lim_{\gamma \rightarrow \infty} S_{div_2} \rightarrow \frac{-1}{4\Lambda}$  (see the thick continuouse line in the left panel of Fig. 9).

**ModAMax field ( $\eta = -1$ ):** By replacing  $\eta = -1$  in the roots of  $S_{div_1}$ , and  $S_{div_2}$ , we find that there is only one the physical limitation point for ModAMax AdS black holes and it is related to  $S_{div_2}$ . In other words, there is one divergence point for the heat capacity when  $\eta = -1$ . In addition, for different values of the topological constants  $S_{div_2}$  turns to the following three conditions

$$\text{phase transition critical points for ModAMax} \implies \begin{cases} S_{div_2} = \frac{-1-\sqrt{1-192\pi^2\Lambda Q^2e^{-\gamma}}}{8\Lambda}, & k = +1 \\ S_{div_2} = \frac{-\sqrt{1-192\pi^2\Lambda Q^2e^{-\gamma}}}{8\Lambda}, & k = 0 \\ S_{div_2} = \frac{1-\sqrt{1-192\pi^2\Lambda Q^2e^{-\gamma}}}{8\Lambda}, & k = -1 \end{cases}, \quad (59)$$

which indicates that the largest root belongs to  $k = +1$ , and the smallest root is related to  $k = -1$ . In other words, by fixing other values of parameter (such as  $\Lambda$ ,  $Q$ , and  $\gamma$ ), we find that a order for the phase transition critical points which depends on the topological constant as  $S_{div_{2k=-1}} < S_{div_{2k=0}} < S_{div_{2k=+1}}$ . Furthermore, in the limit  $\gamma \rightarrow \infty$ , the phase transition critical point only exist for  $k = +1$ , because

$$\begin{cases} \lim_{\gamma \rightarrow \infty} S_{div_2} \rightarrow \frac{-1}{4\Lambda} & k = +1 \\ \lim_{\gamma \rightarrow \infty} S_{div_2} \rightarrow 0 & k = 0 \\ \lim_{\gamma \rightarrow \infty} S_{div_2} \rightarrow 0 & k = -1 \end{cases}. \quad (60)$$

Now we can evaluate the effects of various parameters on the local stability by using the behavior of temperature and heat capacity, simoultanatously. For this purpose, we plot Figs. 9 and 10. Our findings reveal some interesting behaviors which are:

**ModMax field ( $\eta = +1$ ):** Based on different values of the topological constants and for  $\eta = +1$ , we find three categories;

- i) For  $k = +1$  (left panel in Fig. 9), and by considering small values of  $\gamma$ , there are two different areas for the heat capacity. The large ModMax AdS black holes satisfy the local stability condition because in the range  $S > S_{root_2}$ , the heat capacity and the temperature are positive. However, the small ModMax AdS black holes are unstable because the heat capacity is negative in the range  $S < S_{root_2}$  (see dotted and dotted-dashed lines in the left panel of Fig. 9). It is notable that, the local stability area increases when the ModMax parameter increases. There is an interesting behavior for the heat capacity when  $\gamma$  is big. Indeed, there is a critical value for  $\gamma$  ( $\gamma_{critical}$ ), which leads to two divergence points for the heat capacity when  $k = +1$ , and  $\gamma$  is big but follow the condition  $\gamma < \gamma_{critical}$ . In this case, there are three areas for the heat capacity of ModMax AdS black holes (see dashed line in the left panel of Fig. 9); the

first area satisfies the local stability condition and is located in the range  $S > S_{div_2}$ . The second area is located in the range  $S_{div_1} < S < S_{div_2}$ , and the thermodynamical system is unstable due to the negative value of the heat capacity. The third area belongs to stable area and is located in the range  $S < S_{div_1}$ . On the other hand, for  $\gamma > \gamma_{critical}$ , there is one divergence point (which is related to  $S_{div_2}$ , and in the limit  $\gamma \rightarrow \infty$ ,  $S_{div_2} \rightarrow \frac{-1}{4\Lambda}$ ) for the heat capacity which large ModMax AdS black holes can satisfy the local stability condition. In other words, the heat capacity is positive (negative) in the range  $S > S_{div_2}$  ( $S < S_{div_2}$ ), see continuous line in the left panel of Fig. 9.

- ii) For  $k = 0$  (middle panel in Fig. 9), there is one real positive root of the heat capacity ( $S_{root_2}$ ) which determines stable and unstable areas. Indeed, for  $k = 0$ , the ModMax AdS black holes satisfy the local stability condition when  $S > S_{root_2}$ , whereas the small black holes ( $S < S_{root_2}$ ) are unstable thermal objects because the heat capacity is negative when  $S < S_{root_2}$ . Also, there is a critical value for  $\gamma$  ( $\gamma_{critical}$ ), which by considering  $\gamma < \gamma_{critical}$ , the root of the heat capacity decreases by increasing  $\gamma$  which leads to increase the stable area. But for  $\gamma > \gamma_{critical}$  this root disappears and ModMax AdS black holes are stable thermodynamics objects with any radius.
- iii) For  $k = -1$ , (right panel in Fig. 9), there is always one real positive root of the heat capacity ( $S_{root_2}$ ) even in the limit  $\gamma \rightarrow \infty$  (i.e.,  $\lim_{\gamma \rightarrow \infty} S_{root_2} \rightarrow \frac{-1}{4\Lambda}$ ). By considering  $k = -1$ , the ModMax AdS black holes are stable and unstabel thermal objects when  $S > S_{root_2}$  and  $S < S_{root_2}$ , respectively. It is notable that, the local stability area increases by increasing  $\gamma$ .

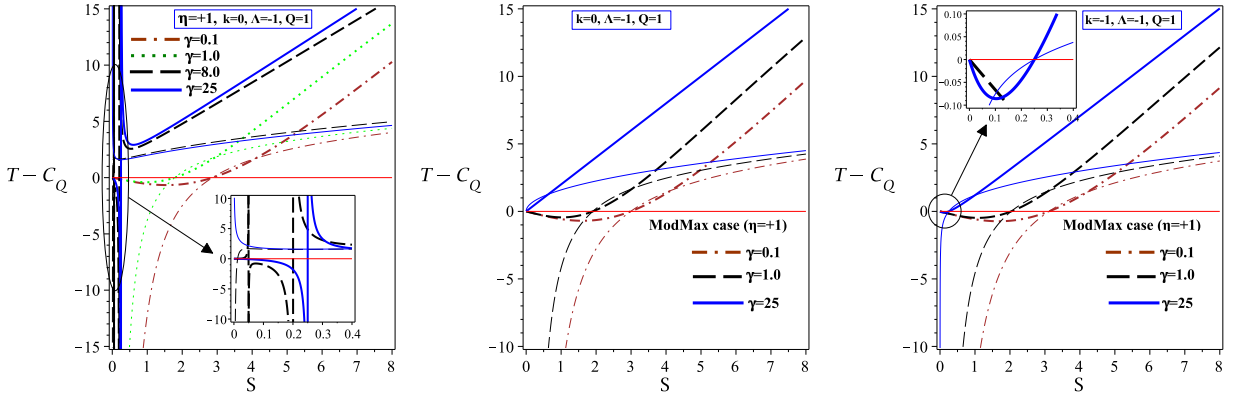


FIG. 9: The Hawking temperature  $T$  (thin lines) and the heat capacity  $C_Q$  (thick lines) versus entropy  $S$  for  $k = +1$  (left panel),  $k = 0$  (middle panel), and  $k = -1$  (right panel) by considering the ModMax field ( $\eta = +1$ ).

**ModAMax field ( $\eta = -1$ ):** There exists a critical value for the ModMax parameter, denoted as  $\gamma_{critical}$ , which dictates a qualitative change in the behavior of the heat capacity ( $C_Q$ ).

- i) For  $\gamma < \gamma_{critical}$ : A single divergence point for the heat capacity,  $S_{div_2}$ , exists, contingent on the topological constant ( $k$ ). In the regime  $S < S_{div_2}$ , the heat capacity  $C_Q$  is negative, indicating thermodynamic instability. These configurations correspond to small ModAMax AdS black holes. In the regime  $S > S_{div_2}$ , the heat capacity is positive, implying local thermodynamic stability (as illustrated by the dashed and dash-dotted lines in Fig. 10). As  $\gamma$  increases within this range, the divergence point  $S_{div_2}$  shifts toward lower entropy values. This effectively means that increasing  $\gamma$  enhances the local stability of the system.
- ii) For  $\gamma > \gamma_{critical}$ : The thermal behavior is strongly dependent on the topological constant  $k$ . For  $k = +1$ , the divergence point  $S_{div_2}$  persists, with  $\lim_{\gamma \rightarrow \infty} S_{div_2} \rightarrow \frac{-1}{4\Lambda}$ . For  $k = 0$ , the heat capacity  $C_Q$  remains positive across all entropy values (as shown by the continuous line in the middle panel of Fig. 10). Consequently, ModAMax AdS black holes in this configuration always satisfy the local stability criterion, irrespective of their entropy. For  $k = -1$ , a root for the heat capacity,  $S_{root_2}$ , appears where  $C_Q$  changes sign. Specifically,  $C_Q < 0$  for  $S < S_{root_2}$  (unstable small black holes), and  $C_Q > 0$  for  $S > S_{root_2}$  (locally stable large black holes), as depicted by the solid line in the right panel of Fig. 10. Thus, for  $k = -1$ , local stability is achieved once the black hole radius (or entropy) is sufficiently large.

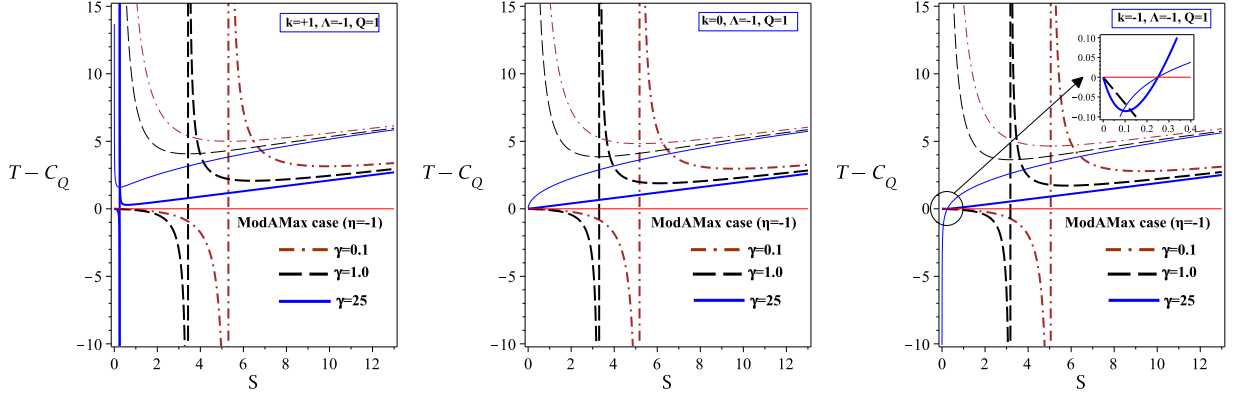


FIG. 10: The Hawking temperature  $T$  (thin lines) and the heat capacity  $C_Q$  (thick lines) versus entropy  $S$  for  $k = +1$  (left panel),  $k = 0$  (middle panel), and  $k = -1$  (right panel) by considering the ModAMax field ( $\eta = -1$ ).

## B. Global Stability

In the grand-canonical ensemble, the global thermodynamic stability is ascertained by examining the Gibbs free energy potential ( $G$ ); specifically, a negative sign for this potential ensures global stability. Concurrently, within the canonical ensemble, the global stability criterion is satisfied by the negative of the Helmholtz free energy ( $F$ ). Consequently, we employ the Gibbs and Helmholtz free energies to systematically evaluate the global stability properties of the topological Mod(A)Max AdS black holes.

It is notable that in the usual case of thermodynamics the Helmholtz free energy is given by  $F = U - TS$ . However, in the context of the black holes, Helmholtz free energy is defined in the following form

While the conventional thermodynamic definition for the Helmholtz free energy is given by  $F = U - TS$ , it is crucial to note that within the context of black hole thermodynamics, this potential is redefined as follows

$$F = M(S, Q) - TS, \quad (61)$$

by using Eqs. (49) and (50) within Eq. (61), we get the Helmholtz free energy in the following form

$$F = \frac{4\Lambda S^2 + 3kS + 36\pi^2\eta Q^2 e^{-\gamma}}{24\pi\sqrt{S}}, \quad (62)$$

and by solving  $F = 0$ , we can obtain the real positive root of the Helmholtz free energy which is as

$$S_{F=0} = \frac{3k + 3\sqrt{k^2 - 64\pi^2\Lambda\eta Q^2 e^{-\gamma}}}{-8\Lambda}, \quad (63)$$

which for different topological constant we have

$$S_{F=0} = \begin{cases} \frac{3+3\sqrt{1-64\pi^2\Lambda\eta Q^2 e^{-\gamma}}}{-8\Lambda}, & k = +1 \\ \frac{3\sqrt{-64\pi^2\Lambda\eta Q^2 e^{-\gamma}}}{-8\Lambda}, & k = 0 \\ \frac{-3+3\sqrt{1-64\pi^2\Lambda\eta Q^2 e^{-\gamma}}}{-8\Lambda}, & k = -1 \end{cases} \quad (64)$$

The largest and smallest real positive roots associated with the Helmholtz free energy correspond to the topological indices  $k = +1$ , and  $k = -1$ , respectively. Under the condition of a negative cosmological constant ( $\Lambda < 0$ ), the existence of roots for the ModAMax AdS black holes is determined by the specific thermodynamic potential being analyzed. More specifically, for the case  $\eta = +1$ , exactly one real, positive root is identified for the Helmholtz free energy ( $F = 0$ ). To characterize the area of global thermodynamic stability for the Mod(A)Max AdS black holes, we present a plot of  $F$  versus the entropy ( $S$ ) in Fig. 11. Our findings reveal two critical points related to the effect of  $\gamma$ , which are

**ModMax field ( $\eta = +1$ ):** Similar to preceding analyses, a critical value for the ModMax parameter ( $\gamma_{critical}$ ) demarcates two distinct stability behaviors: i) For  $\gamma < \gamma_{critical}$ : The Helmholtz free energy exhibits a sign change at  $S_{F=0}$ , being negative for  $S > S_{F=0}$  and positive for  $S < S_{F=0}$ . Consequently, large ModMax AdS black holes satisfy the global stability condition ( $F < 0$ ) when  $S > S_{F=0}$  (as indicated by the dotted-dashed and dashed bold lines in Fig. 11). Furthermore, increasing the ModMax parameter expands this region of global stability. ii) For  $\gamma > \gamma_{critical}$  and  $k = +1$ : Only one real root exists for the Helmholtz free energy. Global stability is satisfied for ModMax AdS black holes when  $S > S_{F=0}$  (shown by the continuous thick line in the left panel of Fig. 11). Cases  $k = 0$ , and  $k = -1$ : No real root exists for  $F$ . In these scenarios,  $F$  remains strictly negative across all relevant physical horizons. Therefore, ModMax AdS black holes with zero ( $k = 0$ ) and negative ( $k = -1$ ) topological indices inherently respect the global stability criterion ( $F < 0$ ) (illustrated in the thick lines in the middle and right panels of Fig. 11).

**ModAMax field ( $\eta = -1$ ):** In this regime, the Helmholtz free energy for the ModAMax AdS black holes exhibits no real root ( $F \neq 0$ ); consequently, this quantity is strictly negative across all relevant horizons. Thus, the ModAMax AdS black holes intrinsically satisfy the global stability condition. In other words,  $F$  remains negative ( $F < 0$ ) for ModAMax AdS black holes characterized by various topological indices (as shown by the thick lines in Fig. 12).

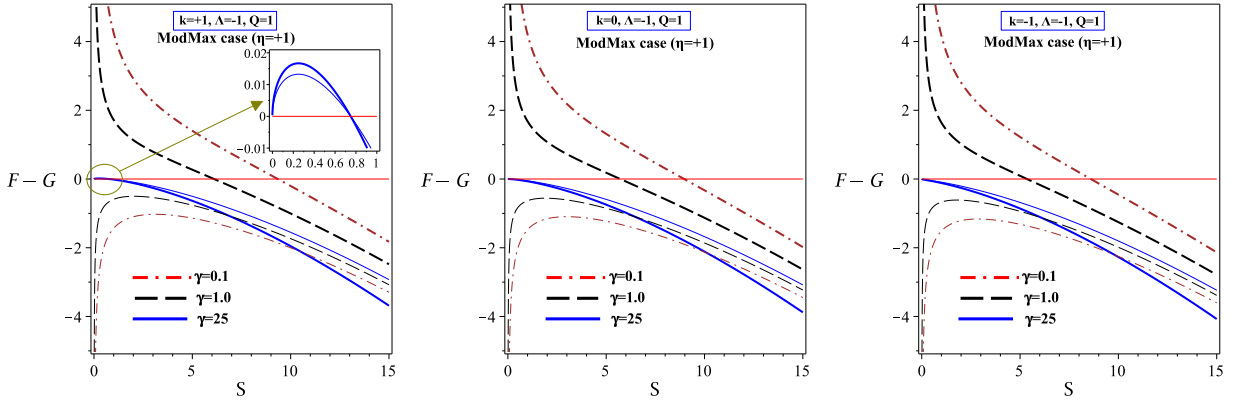


FIG. 11: The Helmholtz free energy  $F$  (thick lines) and the Gibbs free energy  $G$  (thin lines) versus entropy  $S$  for  $k = +1$  (left panel),  $k = 0$  (middle panel), and  $k = -1$  (right panel) by considering the ModMax field ( $\eta = +1$ ).

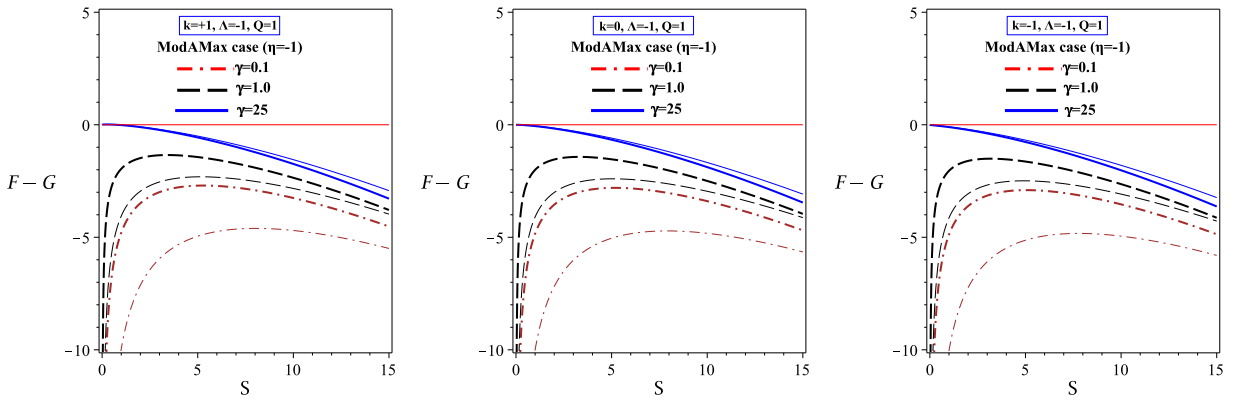


FIG. 12: The Helmholtz free energy  $F$  (thick lines) and the Gibbs free energy  $G$  (thin lines) versus entropy  $S$  for  $k = +1$  (left panel),  $k = 0$  (middle panel), and  $k = -1$  (right panel) by considering the ModAMax field ( $\eta = -1$ ).

The Gibbs free energy (or Gibbs potential) is defined in the following form

$$G = M(S, Q) - TS - \eta UQ, \quad (65)$$

by applying  $U = \left( \frac{\partial M(S, Q)}{\partial Q} \right)_S$ , Eqs. (49) and (50) within Eq. (65), we can obtain the Gibbs free energy as

$$G = \frac{4\Lambda S^2 + 3kS + 48\pi^2 \left( \frac{3}{4} - \eta \right) Q^2 e^{-\gamma}}{24\pi\sqrt{S}}. \quad (66)$$

To determine the point of thermodynamic equilibrium, the equation  $G = 0$  must be solved. Analysis of the resulting solutions indicated that there is only one real positive root for  $\eta = +1$  (ModMax field), and  $k = +1$ , which is in the following form

$$S_{G=0} = \frac{3 + \sqrt{9 + 192\pi^2 \Lambda Q^2 e^{-\gamma}}}{-8\Lambda}, \quad (67)$$

this root is positive when  $\gamma$  includes very large values (see the continuous thin line in the left panel of Fig. 11). It is notable that, the global thermodynamic stability is therefore established by the condition  $G < 0$ . To rigorously evaluate the global stability criterion for these black holes, we present the results in Figs. 11 and 12, which are organized into six distinct panels. Our findings reveals that:

**ModMax field ( $\eta = +1$ ):** For the case  $k = +1$ , a critical value for the ModMax parameter,  $\gamma_{critical}$ , dictates the existence of a real, positive root for the Gibbs free energy ( $G = 0$ ). When  $\gamma < \gamma_{critical}$ , the Gibbs free energy remains negative ( $G < 0$ ); consequently, the ModMax AdS black holes always satisfy the global stability condition. Conversely, when  $\gamma > \gamma_{critical}$ , a single real, positive root for  $G = 0$  emerges, which defines the transition between negative and positive regions of  $G$ . Specifically,  $G$  is negative (positive) when  $S > S_{G=0}$  ( $S < S_{G=0}$ ), as illustrated by the continuous thin line in the left panel of Fig. 11. For the topological constants  $k = 0$ , and  $k = -1$ , the Gibbs free energy is invariably negative ( $G < 0$ ), ensuring that the ModMax AdS black holes satisfy the global stability criterion across all relevant parameter values (see the thin lines in the middle and right panels of Fig. 11).

**ModAMax field ( $\eta = -1$ ):** In this scenario, no real root for the Gibbs free energy ( $G = 0$ ) exists, and the potential remains negative ( $G < 0$ ) across all physically relevant radii. Consequently, the ModAMax AdS black holes inherently satisfy the global stability condition (as depicted by the thin lines in Fig. 12).

## V. JOULE–THOMSON EXPANSION

During a Joule–Thomson expansion, a gas flows from a high-pressure area through a porous plug or small valve into a lower-pressure section of a thermally insulated tube, maintaining a constant enthalpy throughout the process. The resulting temperature change as a function of pressure is described by

$$\mu_J = \left( \frac{\partial T}{\partial P} \right)_H, \quad (68)$$

where  $\mu_J$  is a Joule–Thomson coefficient. One can predict whether the gas will cool or heat by examining the sign of  $\mu_J$ . In a Joule–Thomson expansion, the pressure always decreases, meaning the change in pressure is negative; however, the temperature change can be either positive or negative. If the temperature decreases, the Joule–Thomson coefficient is positive, indicating that the gas cools.

The Joule–Thomson coefficient can be derived by expressing the fundamental thermodynamic relations in terms of volume and heat capacity at constant pressure. For a system with a fixed number of particles  $N$ , the first law of thermodynamics gives

$$dM = dH = TdS + VdP + \eta UdQ. \quad (69)$$

In a Joule–Thomson expansion, enthalpy is constant ( $dH = 0$ ) and any non-mechanical work is assumed to be zero, which leads to

$$T \left( \frac{\partial S}{\partial P} \right)_H + V = 0. \quad (70)$$

Because the entropy  $S$  is a state function, its differential can be written as

$$dS = \left( \frac{\partial S}{\partial P} \right)_T dT + \left( \frac{\partial S}{\partial T} \right)_P dP. \quad (71)$$

Thus, the partial derivative of entropy with respect to pressure at constant enthalpy can be written:

$$\left( \frac{\partial S}{\partial P} \right)_H = \left( \frac{\partial S}{\partial P} \right)_T \left( \frac{\partial T}{\partial P} \right)_H + \left( \frac{\partial S}{\partial T} \right)_P. \quad (72)$$

Substituting Eq. (72) into Eq. (70), gives

$$T \left[ \left( \frac{\partial S}{\partial P} \right)_T + \left( \frac{\partial S}{\partial T} \right)_P \left( \frac{\partial T}{\partial P} \right)_H \right] + V = 0. \quad (73)$$

Applying the Maxwell relation  $\frac{C_P}{T} = \left( \frac{\partial S}{\partial T} \right)_P$  and the identity  $\left( \frac{\partial S}{\partial T} \right)_T = - \left( \frac{\partial V}{\partial T} \right)_P$ , we obtain

$$-T \left( \frac{\partial V}{\partial T} \right)_P + C_P \left( \frac{\partial T}{\partial P} \right)_H + V = 0, \quad (74)$$

which can be rearranged to give the Joule-Thomson coefficient

$$\mu_J = \left( \frac{\partial T}{\partial P} \right)_H = \frac{1}{C_P} \left[ T \left( \frac{\partial V}{\partial T} \right)_P - V \right]. \quad (75)$$

Eq. (75) shows that the sign of  $\mu_J$  is determined by the bracketed term, which yields the classical inversion curve where  $\mu_J = 0$ , while the magnitude and possible divergence of  $\mu_J$  are controlled by the factor  $1/C_P$ . The notation  $C_P$  may also be written as  $C_{P,Q}$  to emphasize that, during a Joule–Thomson expansion, the heat capacity is evaluated at constant pressure and fixed electric charge. The appearance of  $C_P$  follows directly from the isoenthalpic condition of the process and from the first law of thermodynamics; other heat capacities, such as  $C_V$  do not enter the analysis of the Joule-Thomson effect.

The expression (75) makes two features explicit:

- $C_P \rightarrow 0$  : this occurs when  $T \rightarrow 0$ . In this regime  $|\mu_J| \rightarrow \infty$ , as expected near extremality.
- $C_P \rightarrow \infty$  : this occurs at second-order phase transitions. In this limit,  $\mu_J \rightarrow 0$  regardless of the value of the bracketed term in Eq. 75. Hence, the inversion condition  $\mu_J = 0$  can be satisfied trivially due to the divergence of  $C_P$ , a mechanism distinct from the classical inversion curve where  $T(\partial V/\partial T)_P = V$ . This behavior underscores that near critical points, the dominant thermodynamic anomaly is caloric rather than volumetric.

Setting  $T \left( \frac{\partial V}{\partial T} \right)_P - V = 0$ , yields the condition for the inversion temperature, beyond which the sign of  $\mu_J$  changes and the transition between heating and cooling occurs. The inversion temperature is therefore expressed as

$$T_i = V \left( \frac{\partial T}{\partial V} \right)_P. \quad (76)$$

As is well known, the thermodynamic pressure is related to the cosmological constant through

$$P = -\frac{\Lambda}{8\pi}. \quad (77)$$

By substituting this relation into the expression for the black hole mass, one can rewrite the mass in the form

$$M = \frac{kr_+}{8\pi} + \frac{Pr_+^3}{3} + \frac{\eta q^2 e^{-\gamma}}{8\pi r_+} = \begin{cases} \frac{kr_+}{8\pi} + \frac{Pr_+^3}{3} + \frac{q^2 e^{-\gamma}}{8\pi r_+}, & \text{ModMax} \\ \frac{kr_+}{8\pi} + \frac{Pr_+^3}{3} - \frac{q^2 e^{-\gamma}}{8\pi r_+}, & \text{ModAMax} \end{cases}. \quad (78)$$

TABLE I: Solutions of the divergence condition.

Model	Topology ( $k$ )	$r_{+div\mu_J}$
ModMax ( $\eta = +1$ )	+1	$6\pi M + \sqrt{36\pi^2 M^2 - 2q^2 e^{-\gamma}}$
	0	$\frac{q^2 e^{-\gamma}}{6\pi M}$
	-1	$-6\pi M + \sqrt{36\pi^2 M^2 + 2q^2 e^{-\gamma}}$
ModAMax ( $\eta = -1$ )	+1	$6\pi M + \sqrt{36\pi^2 M^2 + 2q^2 e^{-\gamma}}$
	0	Does Not Exist
	-1	Does Not Exist

which is taken as the enthalpy  $H$  of the system. Next, by substituting the pressure relation (77) into the expression for the temperature, we obtain

$$P = \frac{T}{2r_+} - \frac{k}{8\pi r_+^2} + \frac{\eta q^2 e^{-\gamma}}{8\pi r_+^4} = \begin{cases} \frac{T}{2r_+} - \frac{k}{8\pi r_+^2} + \frac{q^2 e^{-\gamma}}{8\pi r_+^4}, & \text{ModMax} \\ \frac{T}{2r_+} - \frac{k}{8\pi r_+^2} - \frac{\eta q^2 e^{-\gamma}}{8\pi r_+^4}, & \text{ModAMax} \end{cases}.$$

With these expressions at hand, we now employ the definition of the Joule–Thomson coefficient (68) to determine its explicit form.

$$\mu_J = \frac{\frac{4k}{r_+^2} + \frac{16\pi P}{3} - \frac{6\eta q^2 e^{-\gamma}}{r_+^4}}{4\pi \left( \frac{3k}{8\pi r_+^3} + \frac{3P}{r_+} - \frac{3\eta q^2 e^{-\gamma}}{8\pi r_+^5} \right)} = \begin{cases} \frac{\frac{4k}{r_+^2} + \frac{16\pi P}{3} - \frac{6\eta q^2 e^{-\gamma}}{r_+^4}}{4\pi \left( \frac{3k}{8\pi r_+^3} + \frac{3P}{r_+} - \frac{3\eta q^2 e^{-\gamma}}{8\pi r_+^5} \right)}, & \text{ModMax} \\ \frac{\frac{4k}{r_+^2} + \frac{16\pi P}{3} + \frac{6\eta q^2 e^{-\gamma}}{r_+^4}}{4\pi \left( \frac{3k}{8\pi r_+^3} + \frac{3P}{r_+} + \frac{3\eta q^2 e^{-\gamma}}{8\pi r_+^5} \right)}, & \text{ModAMax} \end{cases}. \quad (79)$$

To investigate the divergence of the Joule–Thomson coefficient in terms of the black hole mass, we eliminate the thermodynamic pressure using the enthalpy relation. Substituting  $P$  ( $P \rightarrow M, r_+$ ) into the above expression yields

$$\mu_J = \frac{\frac{2k}{r_+^2} + \frac{16\pi M}{r_+^3} - \frac{8\eta q^2 e^{-\gamma}}{r_+^4}}{4\pi \left( \frac{9M}{r_+^4} - \frac{6k}{8\pi r_+^3} - \frac{3\eta q^2 e^{-\gamma}}{2\pi r_+^5} \right)} = \begin{cases} \frac{\frac{2k}{r_+^2} + \frac{16\pi M}{r_+^3} - \frac{8\eta q^2 e^{-\gamma}}{r_+^4}}{4\pi \left( \frac{9M}{r_+^4} - \frac{6k}{8\pi r_+^3} - \frac{3\eta q^2 e^{-\gamma}}{2\pi r_+^5} \right)}, & \text{ModMax} \\ \frac{\frac{2k}{r_+^2} + \frac{16\pi M}{r_+^3} + \frac{8\eta q^2 e^{-\gamma}}{r_+^4}}{4\pi \left( \frac{9M}{r_+^4} - \frac{6k}{8\pi r_+^3} + \frac{3\eta q^2 e^{-\gamma}}{2\pi r_+^5} \right)}, & \text{ModAMax} \end{cases}. \quad (80)$$

The divergence of  $\mu_J$  occurs when the denominator vanishes. Solving this condition for  $r_+$  at fixed mass leads to the quadratic equation:

$$kr_+^2 - 12\pi Mr_+ + 2\eta q^2 e^{-\gamma} = 0. \quad (81)$$

The real and positive roots of this equation define the physical horizon radii at which  $\mu_J$  becomes singular. This indicates that the presence of a divergence is highly sensitive to both the topology  $k$  and the NED parameter  $\eta$ . Since the equation is quadratic in  $r_+$ , it can yield up to two mathematical roots; however, only real and positive solutions correspond to physical black holes. The specific roots depend explicitly on  $k$  and  $\eta$ . For spherical topology ( $k = +1$ ), the discriminant indicates whether a divergence exists. In flat topology ( $k = 0$ ), a single positive root emerges for ModMax black holes. In the hyperbolic case ( $k = -1$ ), ModMax ( $\eta = +1$ ) consistently yields a real root, while ModAMax ( $\eta = -1$ ) results in negative or complex solutions, thus preventing a physical divergence. These findings are summarized in the table below.

We aim to investigate how the Joule–Thomson coefficient  $\mu_J$  varies with the horizon radius  $r_+$  for different black hole masses  $M$  within the Mod(A)Max framework. To demonstrate this relationship,  $\mu_J$  is plotted against  $r_+$  in Figs. 13 and 14.

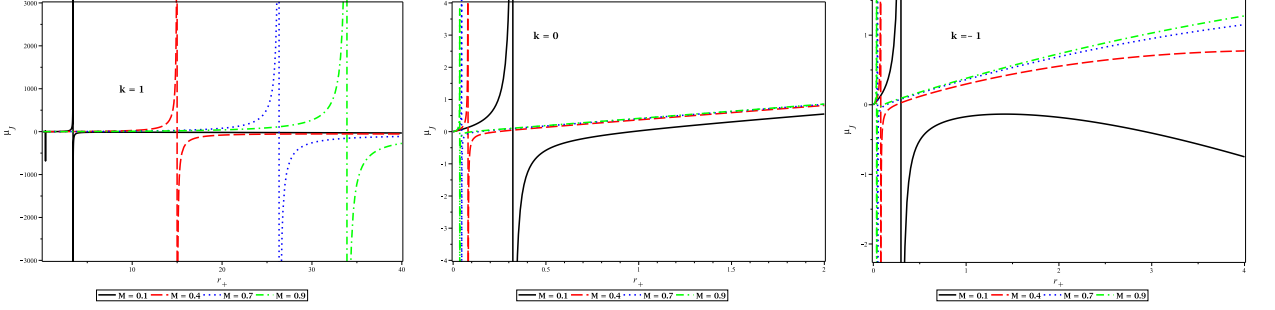


FIG. 13: Joule-Thomson coefficient  $\mu_J$  with respect  $r_+$ , and different values of the ModMax's parameters. Here we take:  $q = 1$  and  $\gamma = 0.5$

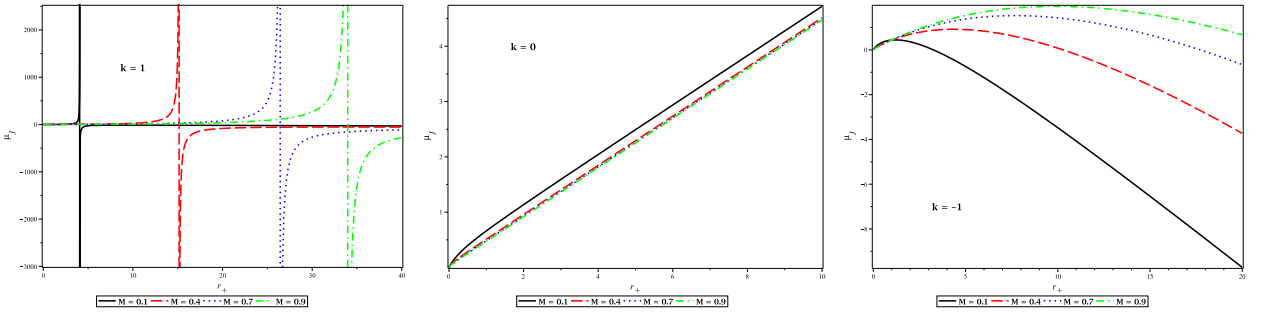


FIG. 14: Joule-Thomson coefficient  $\mu_J$  with respect  $r_+$ , and different values of the ModAMax's parameters. Here we take:  $q = 1$  and  $\gamma = 0.5$

**ModMax ( $\eta = +1$ ):** In this case, the Joule-Thomson coefficient  $\mu_J$  also exhibits a well-defined inversion point separating the cooling and heating regimes. However, the *critical distinction among the topological classes* is governed by the influence of the black hole mass  $M$ . For  $k = +1$ , increasing the mass systematically shifts the inversion point toward larger critical horizon radii, reflecting the enhancement of the gravitational field strength. Conversely, for  $k = 0$  and  $k = -1$ , the trend is inverted: increasing the mass shifts the inversion point toward smaller critical horizon radii.

**ModAMax ( $\eta = -1$ ):** For the spherical topology ( $k = +1$ ),  $\mu_J$  exhibits a well-defined inversion point, separating the cooling and heating regions in a manner similar to the ModMax case. In the flat topology ( $k = 0$ ),  $\mu_J$  remains positive for all values of  $r_+$ , indicating that the system stays in a continuous cooling phase with no inversion point. However, for the hyperbolic topology ( $k = -1$ ),  $\mu_J$  is initially positive for small  $r_+$ , corresponding to a cooling regime, and then becomes negative as  $r_+$  increases, signaling a transition from cooling to heating. This reveals that hyperbolic ModAMax black holes exhibit a mixed thermodynamic behavior, where both cooling and heating phases coexist depending on the horizon radius. Overall, the results demonstrate that the topology parameter  $k$  strongly influences the thermal characteristics of ModAMax AdS black holes and that the transition behavior for  $k = -1$  is qualitatively distinct from the other topological cases.

The condition  $\mu_J = 0$  applied to Eq.(79) , gives

$$8\pi P_i r_+^4 + 6kr_+^2 - 9\eta q^2 e^{-\gamma} = 0. \quad (82)$$

Solving this quartic equation for  $r_+$  yields four roots; however, only one of them is physically acceptable, as the others are either complex or negative. The positive real root is given by

$$r_+ = r_i = \sqrt{-\frac{3k}{8\pi P_i} + \frac{3\sqrt{k^2 + 8\pi P_i q^2 \eta e^{-\gamma}}}{8\pi P_i}} = \begin{cases} \sqrt{-\frac{3k}{8\pi P_i} + \frac{3\sqrt{k^2 + 8\pi P_i q^2 e^{-\gamma}}}{8\pi P_i}}, & \text{ModMax} \\ \sqrt{-\frac{3k}{8\pi P_i} + \frac{3\sqrt{k^2 - 8\pi P_i q^2 e^{-\gamma}}}{8\pi P_i}}, & \text{ModAMax} \end{cases}, \quad (83)$$

TABLE II: Summary of Joule–Thomson inversion behavior and minimum quantities for topological Mod(A)Max AdS black holes.

Model	Topology ( $k$ )	$\mu_J$ Sign Change	Inversion Point?	$T_i^{\min}$	$M_i^{\min}$
ModMax ( $\eta = +1$ )	+1	Yes	Yes	$\frac{1}{12\pi} \sqrt{\frac{2}{3q^2 e^{-\gamma}}}$	$\frac{5}{24\pi} \sqrt{\frac{3q^2 e^{-\gamma}}{2}}$
	0	Yes	Yes	0	0
	-1	Yes	Yes	unphysical	unphysical
ModAMax ( $\eta = -1$ )	+1	Yes	Yes	unphysical	unphysical
	0	No	No	Does Not Exist	Does Not Exist
	-1	Yes	Yes	unphysical	unphysical

where  $P_i$  manifests the inversion pressure. Furthermore, the corresponding expression for the black hole inversion temperature is :

$$T_i = \frac{2Pr_i}{3} - \frac{k}{12\pi r_i} + \frac{\eta e^{-\gamma} q^2}{4\pi r_i^3} = \begin{cases} \frac{2Pr_i}{3} - \frac{k}{12\pi r_i} + \frac{e^{-\gamma} q^2}{4\pi r_i^3}, & \text{ModMax} \\ \frac{2Pr_i}{3} - \frac{k}{12\pi r_i} - \frac{e^{-\gamma} q^2}{4\pi r_i^3}, & \text{ModAMax} \end{cases}. \quad (84)$$

The minimum inversion temperature is obtained by substituting  $r_+ = r_i$  from Eq. (82) and taking  $P_i = 0$  in the above relation, which gives

$$T_i^{\min} = \frac{k}{12\pi} \sqrt{\frac{2k}{3\eta q^2 e^{-\gamma}}}.$$

Correspondingly, the minimum inversion mass is given by

$$M_i^{\min} = \frac{5k}{24\pi} \sqrt{\frac{3\eta q^2 e^{-\gamma}}{2k}}. \quad (85)$$

Table. II presents a comparative summary of the Joule–Thomson inversion behavior and the corresponding minimum quantities for the topological Mod(A)Max AdS black holes. The results show that the existence of a minimum inversion temperature  $T_i^{\min}$  and mass  $M_i^{\min}$  strongly depends on both the electrodynamic model and the horizon topology. In the ModMax case ( $\eta = +1$ ), well-defined and positive values of  $T_i^{\min}$  and  $M_i^{\min}$  appear for the spherical topology ( $k = +1$ ), indicating that these black holes can undergo a cooling phase during the Joule–Thomson expansion. For the flat topology ( $k = 0$ ), the inversion occurs only at zero temperature and mass, while for the hyperbolic case ( $k = -1$ ), the resulting values are unphysical. In contrast, for the ModAMax model ( $\eta = -1$ ), the inversion characteristics are notably different. Although spherical and hyperbolic topologies still exhibit sign changes in  $\mu_J$ , the corresponding minimum inversion quantities are unphysical. For  $k = 0$ , there is no inversion point, and the system remains in a continuous cooling phase.

In Fig. 15 we depicted the inversion temperature  $T_i$  of the ModMax black hole as a function of the inversion pressure  $P_i$  for  $k = 1$ . From this plot, we observe that the inversion temperature increases monotonically with pressure. Notably, unlike conventional thermodynamic systems such as the van der Waals gas, these black holes do not exhibit a maximum inversion temperature. Each curve possesses a minimum inversion temperature  $T_i^{\min}$ , below which inversion does not occur. The region above each curve represents the cooling regime ( $\mu_J > 0$ ), while the area below corresponds to the heating regime ( $\mu_J < 0$ )

## VI. HEAT ENGINES

A black hole heat engine can be mathematically described by a closed  $P – V$  cycle. In this cycle, the system absorbs heat  $Q_H$  from a high-temperature reservoir. As the process unfolds, part of this absorbed heat is converted into mechanical work  $W$ , while the remaining heat  $Q_C$  is released to a lower-temperature reservoir (Fig. 16). Thus, the efficiency  $\Gamma$  of the heat engine is defined as

$$\Gamma = \frac{W}{Q_H}. \quad (86)$$

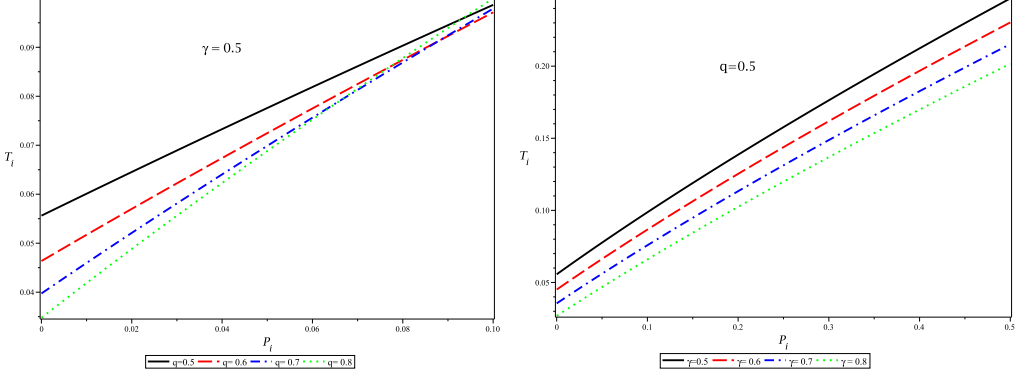


FIG. 15: Inversion temperature  $T_i$  of the ModMax black hole as a function of inversion pressure  $P_i$  for  $k = +1$ .

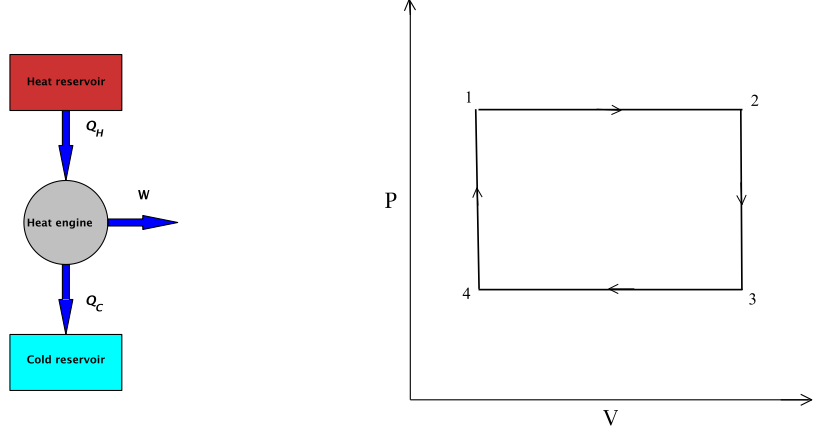


FIG. 16: The figure on the left shows a schematic representation of the heat engine, while the figure on the right illustrates its thermodynamic cycle.

The efficiency of a Carnot engine represents the highest theoretical efficiency that any heat engine can achieve. It is expressed as

$$\Gamma_C = 1 - \frac{Q_C}{Q_H} = 1 - \frac{T_C}{T_H}, \quad (87)$$

where  $T_C$  and  $T_H$  represent the temperatures of the cold and hot reservoirs, respectively. As shown in Fig. 16, the black hole absorbs a quantity of heat  $Q_H$  during isothermal expansion and releases  $Q_C$  during isothermal compression.

To model the Topological Mod(A)Max AdS black hole as a heat engine, we analyze a rectangular thermodynamic cycle in the  $P - V$  plane. This cycle consists of two isobaric and two isochoric processes, illustrated in Fig. 16. The rectangular cycle is favored for its analytical simplicity, as the work done during the isochoric segments is zero. Consequently, the total work output is directly proportional to the area enclosed by the isobaric paths in the  $P - V$  diagram.

Since the paths  $1 \rightarrow 2$  and  $3 \rightarrow 4$  represent isobaric processes, we have  $P_1 = P_2$  and  $P_3 = P_4$ . The total work done during one complete cycle is given by

$$W_{tot} = \oint P dV. \quad (88)$$

Since the segments  $2 \rightarrow 3$  and  $4 \rightarrow 1$  are isochores, their corresponding work contributions are zero. As a

result, the net output work, which geometrically represents the area enclosed by the rectangular cycle, is

$$\begin{aligned} W_{tot} &= W_{1 \rightarrow 2} + W_{3 \rightarrow 4} = P_1 (V_1 - V_2) + P_4 (V_3 - V_4), \\ &= \frac{8}{3} (P_1 - P_4) \left( S_2^{3/2} - S_1^{3/2} \right). \end{aligned} \quad (89)$$

Conversely, the net inflow of heat during the upper isobaric process can be determined from

$$Q_H = \int_T^{T_1} C_P dT = M_2 - M_1, \quad (90)$$

which yields

$$Q_H = \frac{k(\sqrt{S_2} - \sqrt{S_1})}{4\pi} + \frac{8P_1(S_2^{3/2} - S_1^{3/2})}{3} + \frac{\eta q^2 e^{-\gamma} \left( \frac{1}{\sqrt{S_2}} - \frac{1}{\sqrt{S_1}} \right)}{16\pi}. \quad (91)$$

Using Eqs. (89) and (91), we can express the efficiency of this rectangular cycle as follows

$$\Gamma = \frac{\left(1 - \frac{P_4}{P_1}\right)}{1 + \frac{3k(\sqrt{S_2} - \sqrt{S_1})}{32\pi P_1 (S_2^{3/2} - S_1^{3/2})} + \frac{3\eta q^2 e^{-\gamma} \left( \frac{1}{\sqrt{S_2}} - \frac{1}{\sqrt{S_1}} \right)}{128\pi P_1 (S_2^{3/2} - S_1^{3/2})}}. \quad (92)$$

The efficiency of the black hole heat engine, denoted as  $\Gamma$ , can be compared to that of the Carnot engine,  $\Gamma_C$ . By associating the higher temperature  $T_H$  with  $T_2$  and the lower temperature  $T_C$  with  $T_4$ , the Carnot efficiency is expressed as follows

$$\Gamma_C = 1 - \frac{\left(1 + \frac{k}{32\pi P_1 S_2} - \frac{\eta q^2 e^{-\gamma}}{128\pi P_1 S_2^2}\right) \frac{P_1}{P_4} \left(\frac{S_2}{S_1}\right)^{\frac{1}{2}}}{\left(1 + \frac{k}{32\pi P_4 S_1} - \frac{\eta q^2 e^{-\gamma}}{128\pi P_4 S_1^2}\right)}. \quad (93)$$

We have derived the expressions for the efficiency and Carnot efficiency of the black hole heat engine. Now, we are ready to explore how the engine's efficiency and effective efficiency are affected by the various parameters that define the underlying theory.

In Figs. 17 and 18, we illustrate the efficiency of topological Mod(A)Max AdS black holes for various values of  $\gamma$ .

**ModMax ( $\eta = +1$ ):** In the spherical case ( $k = +1$ ), the efficiency increases monotonically with entropy and approaches a constant value as  $S_2$  becomes large. The influence of  $\gamma$  is most pronounced at low entropies, where a larger  $\gamma$  slightly reduces efficiency. However, all curves converge in the high-entropy regime. In contrast, for  $k = 0$  and  $k = -1$ , efficiency decreases as  $S_2$  increases. The dependence on  $\gamma$  is again only noticeable at low entropies and becomes negligible at high  $S_2$ . These findings suggest that NED corrections tend to suppress the efficiency of the ModMax black hole heat engine, particularly for small black holes, while for large black holes, the efficiency becomes nearly independent of both topology and  $\gamma$ .

**ModAMax ( $\eta = -1$ ):** For  $k = +1$  and  $k = 0$ ,  $\Gamma$  increases monotonically with  $S_2$ , approaching an asymptotic value at high entropy. In contrast, for  $k = -1$ ,  $\Gamma$  decreases. In all scenarios, the nonlinear corrections primarily enhance the efficiency of the ModAMax black hole at low  $S_2$ , while the dependence on  $\gamma$  becomes negligible at high entropy.

The plots in Figures 19, and 20 display the variation of the efficiency ratio  $\frac{\Gamma}{\Gamma_C}$  with respect to the entropy  $S_2$  for Mod(A)Max AdS black holes. In both cases, the ratio  $\frac{\Gamma}{\Gamma_C}$  decreases monotonically as  $S_2$  increases, indicating that higher entropies-associated with larger horizon areas or volumes-lead to lower thermodynamic efficiency compared to the Carnot limit. The ModMax parameter  $\gamma$  has no noticeable effect on the efficiency ratio.

The rectangular (isobar-isochoric) cycle is adopted here for its analytical tractability, allowing us to isolate the influence of parameters such as the ModMax coupling  $\gamma$  and the topology parameter  $k$  on work output and

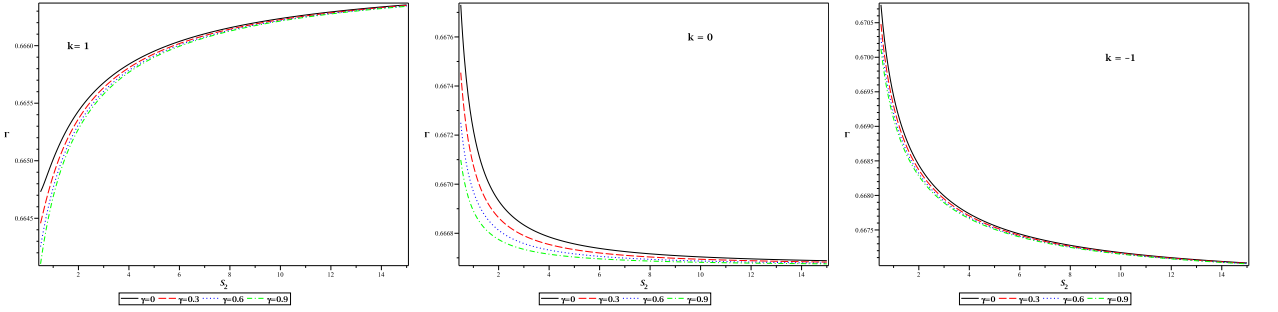


FIG. 17: Plots of the heat engine efficiency  $\Gamma$  as a function of entropy  $S_2$  for the ModMax AdS black hole are presented for various values of  $\gamma$ . In this analysis, we have set  $P_1 = 3$ ,  $P_4 = 1$ ,  $S_1 = 1$ , and  $q = 1$ .

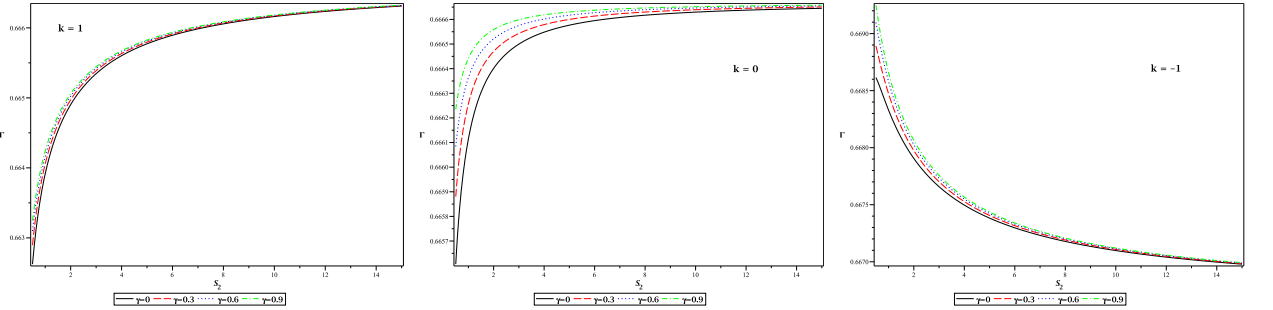


FIG. 18: Plots of the heat engine efficiency  $\Gamma$  as a function of entropy  $S_2$  for the ModAMax AdS black hole are presented for various values of  $\gamma$ . In this analysis, we have set  $P_1 = 3$ ,  $P_4 = 1$ ,  $S_1 = 1$ , and  $q = 1$ .

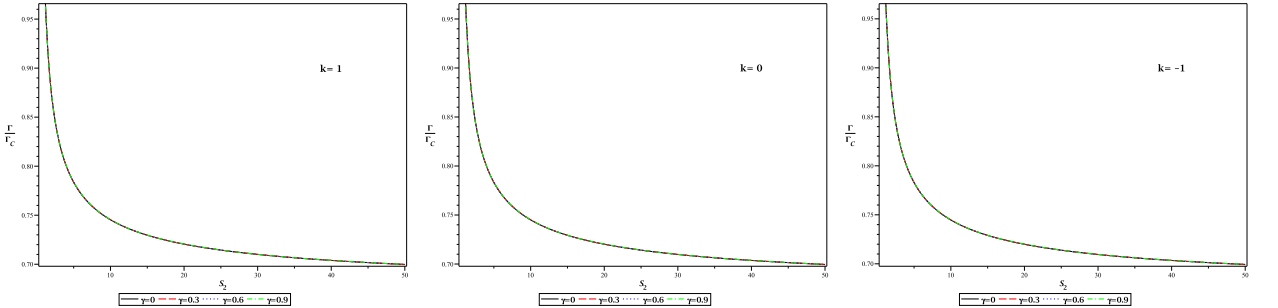


FIG. 19: Plots of the efficiency ratio  $\frac{\Gamma}{\Gamma_C}$  as a function of entropy  $S_2$  for the ModAMax AdS black hole are shown for different values of  $\gamma$ . Here, we set  $P_1 = 3$ ,  $P_4 = 1$ ,  $S_1 = 1$ , and  $q = 1$ .

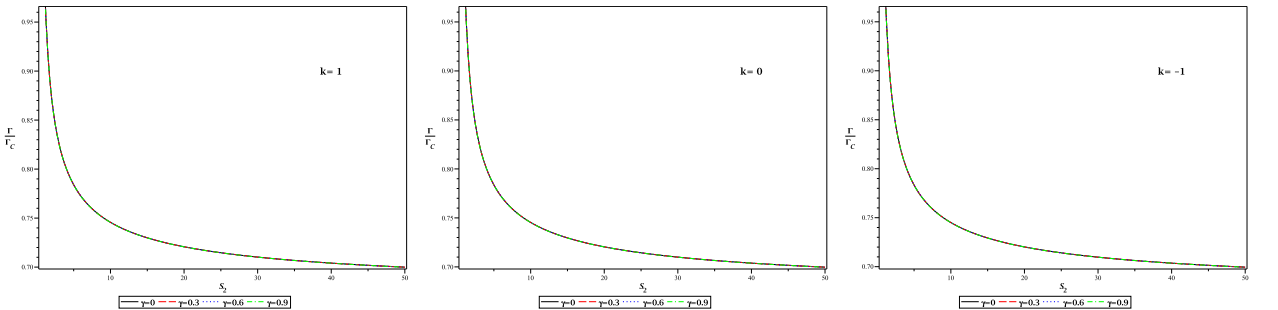


FIG. 20: Plots of the efficiency ratio  $\frac{\Gamma}{\Gamma_C}$  as a function of entropy  $S_2$  for the ModMax AdS black hole are shown for different values of  $\gamma$ . Here, we set  $P_1 = 3$ ,  $P_4 = 1$ ,  $S_1 = 1$ , and  $q = 1$ .

efficiency. Its physical interpretation within extended black-hole thermodynamics, however, indeed warrants explicit clarification.

For the static AdS black holes studied here, both the thermodynamic volume and the Bekenstein–Hawking entropy are monotonic functions of the horizon radius,

$$S = \frac{r_+^2}{4}, \quad V = \frac{r_+^3}{3} \quad \Rightarrow \quad V = \frac{8}{3} S^{3/2}. \quad (94)$$

Hence, an isochoric process ( $V = \text{const}$ ) necessarily fixes  $r_+$  and therefore keeps the entropy constant ( $dS = 0$ ). From the first law (69), it follows that along an isochore with fixed charge one has  $T dS = 0$ . Consequently, all heat transfer occurs exclusively along the isobaric segments, which explains why the mechanical work reduces to the geometric area between the two isobars in the  $P$ – $V$  plane.

It should also be emphasized that this cycle is an idealization. A quasi-static variation of the thermodynamic pressure  $P$  corresponds to a slow change of the effective cosmological constant, describing a continuous path through a family of equilibrium AdS spacetimes. Such cycles therefore serve as theoretical probes of the thermodynamic structure rather than operational protocols.

In addition, the fundamental Carnot bound,  $\eta_C = 1 - \frac{T_C}{T_H}$ , provides the universal upper limit. For the rectangular cycle we identify  $T_H = T(P_1, S_2)$  and  $T_C = T(P_4, S_1)$ . As required by the second law, all efficiencies computed in the manuscript satisfy  $\Gamma < \Gamma_C$ . This has been verified numerically for representative parameter, across a range of  $S_2$  values, as shown in Figures 19 and 20.

To better contextualize the performance of the rectangular cycle and to anticipate how its efficiency compares with theoretically optimal processes, we can consider a Stirling-like cycle composed of two isotherms connected by isochores. In the present framework the isochores coincide with isentropes, so an ideal Stirling cycle would operate reversibly between  $T_H$  and  $T_C$ , thereby attaining the Carnot efficiency  $\Gamma_{\text{Stirling}} \sim \Gamma_C$ . This comparison therefore provides a natural upper benchmark against which the rectangular cycle can be evaluated. As expected, the rectangular cycle is intrinsically less efficient. Nevertheless, its analytical simplicity allows the influence of physical parameters, most notably the ModMax coupling  $\gamma$  and the horizon topology  $k$ , to be identified with clarity. This trade-off between conceptual transparency and optimal performance is typical of model cycles in exploratory black hole thermodynamics and motivates our choice of the rectangular cycle as a diagnostic tool.

## VII. CONCLUSIONS

In this paper, we introduced a coupling between a new modification of Maxwell theory (ModMax) and the anti-Maxwell (phantom) field within the Einstein–Hilbert action, including the cosmological constant. We then derived the corresponding field equations. By examining topological spacetime, we obtained AdS black hole solutions that incorporate both ModMax and ModAMax (modified anti-Maxwell) fields. We refer to these solutions as topological Mod(A)Max black holes. This was the first attempt to combine the phantom field into a NED theory.

We investigated the effects of ModMax’s parameter  $\gamma$ , phantom field  $\eta$ , and topological constant  $k$  on AdS black holes. Notably,  $\eta$  can take values of  $\pm 1$ :  $\eta = +1$  corresponds to the Maxwell field, while  $\eta = -1$  pertains to the anti-Maxwell (phantom) field. Our analysis revealed that ModMax AdS black holes can exhibit two roots, where the smaller root is associated with the inner horizon, and the larger root corresponds to the event horizon. Importantly, as  $\gamma$  increases, the number of roots for ModMax AdS black holes decreases from two to one. Furthermore, smaller black holes are related to a positive topological constant ( $k = +1$ ), while larger black holes correspond to a negative topological constant ( $k = -1$ ). In contrast, ModAMax AdS black holes have only one root, which is linked to the event horizon. Additionally, the event horizon of ModAMax AdS black holes decreases as  $\gamma$  increases. Similar to ModMax black holes, smaller to larger ModAMax black holes are associated with  $k = +1$ ,  $k = 0$ , and  $k = -1$ , respectively. Our analysis of the behavior of Mod(A)Max black holes highlighted two distinct behaviors between ModMax and ModAMax black holes: i) ModMax AdS black holes can have two roots, while ModAMax AdS black holes have only one root; ii) Increasing  $\gamma$  results in an increase in the event horizon for ModMax AdS black holes, whereas the event horizon of ModAMax AdS black holes decreases as  $\gamma$  increases.

We calculated the conserved and thermodynamic quantities for Mod(A)Max AdS black holes, including the Hawking temperature. Our analysis showed that small ModMax AdS black holes can have a negative temperature when  $k = 0$  or  $k = -1$ . In contrast, for  $k = +1$ , the temperature is positive if  $q^2 e^{-\gamma} < r_+^2$ . Furthermore, for small ModAMax black holes, the Hawking temperature is always positive when  $k = +1$  or  $k = 0$ . However, for  $k = -1$ , it is positive only if  $q^2 e^{-\gamma} > r_+^2$ . For large Mod(A)Max black holes, the Hawking temperature depends solely on the cosmological constant and is always positive.

We calculated the total mass of the topological Mod(A)Max black holes. In the high-energy limit, the total mass depends solely on the electrodynamic field. Specifically, we found that the mass of small ModMax AdS black holes can be positive, whereas the total mass of small ModAMax black holes cannot be positive. This distinction is the primary difference between the masses of ModMax and ModAMax black holes. In the asymptotic limit, the total mass relies only on the cosmological constant, indicating that the total mass of large Mod(A)Max AdS black holes is always positive. Indeed, the mass of large Mod(A)Max black holes is positive, which is consistent with the positive Hawking temperature of these black holes.

A simultaneous evaluation of temperature and heat capacity behavior allowed us to analyze the local stability of Mod(A)Max AdS black holes across various topological constants ( $k$ ) and ModMax parameter ( $\gamma$ ) values. The results demonstrated that:

i) **ModMax case:** For  $k = +1$ , small  $\gamma$  yielded an instability region ( $S < S_{root_2}$ ) alongside a stable region for larger entropy, where increasing  $\gamma$  enhanced stability. Critically, for a large  $\gamma < \gamma_{critical}$ , two divergence points resulted in three distinct thermal regimes, while for  $\gamma > \gamma_{critical}$ , only one divergence point remained, causing large black holes to satisfy stability. For  $k = 0$ , stability was maintained when  $S > S_{root_2}$ , but this root disappeared entirely when  $\gamma > \gamma_{critical}$ , rendering all black holes stable. Finally, for  $k = -1$ , a single positive heat capacity root existed across all  $\gamma$ , where stability was always achieved only for sufficiently large entropy values ( $S > S_{root_2}$ ). Overall, increasing  $\gamma$  consistently led to an expansion of the locally stable region for the black hole system.

ii) **ModAMax case:** The investigation revealed that a critical value of the ModMax parameter ( $\gamma_{critical}$ ) influenced the heat capacity ( $C_Q$ ) behavior. When  $\gamma < \gamma_{critical}$ , a divergence point  $S_{div_2}$  existed, separating unstable (small) and stable (large) ModAMax AdS black holes, with increasing  $\gamma$  leading to greater stability overall. Conversely, for  $\gamma > \gamma_{critical}$ , the thermal characteristics depended significantly on the topological constant ( $k$ ). Specifically, for  $k = +1$ ,  $S_{div_2}$  persisted; for  $k = 0$ ,  $C_Q$  remained consistently positive, ensuring stability regardless of entropy; and for  $k = -1$ , the presence of  $S_{root_2}$  dictated stability only for sufficiently large black holes ( $S > S_{root_2}$ ). These observations collectively demonstrated that black hole local stability for  $\eta = -1$  relies on interplay between the topological constant, the ModMax parameter, and, crucially, the black hole's size relative to critical entropy values.

The global stability analysis of Mod(A)Max AdS black holes, investigated via the Helmholtz free energy in the canonical ensemble. Our analysis indicated that:

i) **ModMax case:** For  $\eta = +1$ , a critical parameter  $\gamma_{critical}$  separated the behaviors: below this value, stability ( $F < 0$ ) was achieved only for larger black holes ( $S > S_{F=0}$ ), a domain expanded by increasing  $\gamma$ . Above  $\gamma_{critical}$  with  $k = +1$ , one root existed, yielding stability above  $S_{F=0}$ . Crucially, for  $k = 0$  and  $k = -1$  under  $\eta = +1$ , the Helmholtz free energy possessed no real root and remained strictly negative, inherently ensuring stability.

ii) **ModAMax case:** For  $\eta = -1$ ,  $F$  consistently exhibited no real roots across all  $k$ , leading to universal negativity ( $F < 0$ ). This demonstrated that the existence or non-existence of real roots for the Helmholtz free energy dictated the extent of the thermodynamically stable phase space. Overall, the findings clarified the precise thermodynamic stability boundaries dependent on both the ModMax parameter and the topological constant.

In the grand-canonical ensemble, the global thermodynamic stability for these black holes was rigorously established by the condition  $G < 0$ . Investigation yielded the conclusion that:

i) **ModMax case:** For  $\eta = +1$ , a critical parameter  $\gamma_{critical}$  governed the stability landscape. When  $\gamma < \gamma_{critical}$ ,  $G$  remained negative, intrinsically satisfying stability, while  $\gamma > \gamma_{critical}$  introduced a transition root where stability held only for  $S > S_{G=0}$  when  $k = +1$ . Crucially, for  $k = 0$ , and  $k = -1$  under  $\eta = +1$ ,  $G$  was invariably negative, ensuring global stability across all parameters.

ii) **ModAMax case:** For  $\eta = -1$ , no real root for  $G = 0$  existed, and  $G$  remained universally negative, thus inherently guaranteeing stability.

We also investigated the Joule–Thomson expansion of topological Mod(A)Max AdS black holes in the extended phase space. This analysis yielded explicit expressions for both the Joule–Thomson coefficient and the inversion temperature. Our findings revealed that the inversion curves and the minimum inversion temperature are significantly affected by the NED parameter  $\gamma$  and the topology constant  $k$ .

By modeling these black holes as heat engines operating through a rectangular  $P - V$  cycle, we assessed their efficiency and compared it to the Carnot limit. Our findings indicated that the ModMax and ModAMax parameters, along with the horizon topology, significantly influence the thermodynamic performance of the engine. A notable result is the distinct topological dependence of efficiency: for ModMax black holes, efficiency increases with entropy for spherical topology ( $k = +1$ ) but decreases for both flat ( $k = 0$ ) and hyperbolic ( $k = -1$ ) topologies. In contrast, for ModAMax black holes, efficiency rises with entropy for spherical ( $k = +1$ ) and flat ( $k = 0$ ) topologies, while it decreases in the hyperbolic case ( $k = -1$ ). Additionally, we found that NED corrections reduce the efficiency of small black holes across all configurations.

We emphasise that although our ModAMax solution is obtained through exotic matter, with negative energy density, this does not invalidate it as a possible realistic astrophysical black hole solution. As mentioned in the Introduction, there exist numerous solutions with this exotic-matter feature in GR and in modified gravity theories. Some of them require quantum effects to account for such behaviour. We have shown constraints that render our solutions stable and thermodynamically consistent. In Appendix A, we show that the ModAMax solution with  $k = 1$  may be linearly stable under small geometric perturbations, through the analysis of QNMs using the third-order WKB approximation. Therefore, even the introduction of exotic matter does not necessarily result in instabilities in general. Naturally, we shall need to establish physical constraints on the parameters so that measurements related to astrophysical black holes, such as QPOs, GWs, and EHT observations, may arise from topological ModAMax solutions.

### Acknowledgments

B. Eslam Panah thanks the University of Mazandaran. This work is based upon research funded by Iran National Science Foundation (INSF) under project No.4035285. Manuel E. Rodrigues thanks Conselho Nacional de Desenvolvimento Científico e Tecnológico-CNPq, Brazil, for partial financial support. We extend our gratitude to Professor Vitor Cardoso for the confirmation and valuable references provided regarding the WKB approximation for the Quasi-Normal Modes (QNMs) of the Reissner–Nordström Anti-de Sitter (RN–AdS) solution.

### Appendix A: First perturbative check: scalar modes of the ModAMax solution for $k = +1$

The linear stability analysis of a black hole solution begins by introducing small perturbations to the background metric,  $g_{\mu\nu} \rightarrow g_{\mu\nu} + h_{\mu\nu}$ , where  $h_{\mu\nu}$  denotes an infinitesimal fluctuation. After decomposing these perturbations into spherical harmonics on  $S^2$ , they separate into three main classes according to their transformation properties: scalar modes (spin–0), vector modes (spin–1), and tensor modes (spin–2) [126–130]. Each sector satisfies an independent master equation, typically cast into a radial Schrödinger-type form,

$$\frac{d^2\Psi}{dr_*^2} + [\omega^2 - V_{\text{eff}}(r)] \Psi = 0, \quad (\text{A1})$$

where  $r_*$  is the tortoise coordinate and  $V_{\text{eff}}$  is the associated effective potential [131, 132]. Among these sectors, scalar modes (spin–0) are especially significant in extended or modified theories of gravity, where additional scalar degrees of freedom can produce richer effective potentials, featuring multiple peaks, deep wells, or regions in which the potential becomes negative [133], potentially indicating the presence of unstable or bound-state-type modes.

To investigate dynamical stability, one computes the spectrum of quasi-normal modes (QNMs). With the convention  $\omega = \omega_R + i\omega_I$ , stability requires  $\omega_I < 0$ , ensuring that perturbations decay exponentially in time. When the effective potential exhibits a single smooth barrier, an efficient method for estimating the quasi-normal frequencies is the WKB approximation, originally introduced by Schutz and Will [134] and later extended to higher orders by Iyer and Will [135] and by Konoplya [136]. The  $n$ th-order WKB quantisation condition may be written generically as

$$\frac{i(\omega^2 - V_0)}{\sqrt{-2V_0''}} - \Lambda_n = n + \frac{1}{2}, \quad (\text{A2})$$

where  $V_0 = V_{\text{eff}}(r_{\text{max}})$ ,  $V_0''$  is the second derivative of the potential at its maximum, and  $\Lambda_n$  encodes the higher-derivative corrections [137]. Owing to its accuracy for large angular quantum numbers and single-barrier potentials, the WKB method provides a robust criterion for dynamical stability, permitting one to verify that the imaginary part of the quasi-normal spectrum satisfies  $\omega_I < 0$  for all modes.

The analysis carried out in asymptotically AdS space-times was initially performed in [138, 139] for the Reissner–Nordström–AdS solution. It was concluded that AdS-type solutions indicate stability under linear perturbations. Subsequently, the linear stability of AdS-type solutions was analysed, again suggesting stability [140, 141]. The review [142] shows that these solutions may be analysed using the perturbative WKB method (see Sec. 6), in the limit where the angular momentum number satisfies  $l \gg 1$ , the so-called eikonal limit.

Here we shall carry out this analysis only for the scalar modes (spin  $s = 0$ ) of the ModAMax solution with  $k = 1$ , employing the third-order WKB approximation. This is merely a preliminary analysis indicating the stability of our solution, which may be further improved by enhancing the accuracy (sixth-order WKB and other high-precision methods) and extending the study to higher spins ( $s = 1, 2$ ).

We define the effective potential of the Schrodinger-type equation (A1) for our ModAMax solution following [139]

$$V_{\text{eff}}(r) = (-g_{tt}) \left( \frac{l(l+1)}{g_{\theta\theta}} + \frac{1}{r} \frac{d(-g_{tt})}{dr} \right) = \frac{(r(-3kr + 3m + \Lambda r^3) - 3\eta q^2 e^{-\gamma}) (r(2\Lambda r^3 - 3(l(l+1)r + m)) + 6\eta q^2 e^{-\gamma})}{9r^6}, \quad (\text{A3})$$

where  $g_{tt}$  and  $g_{\theta\theta}$  are the components of the metric (9), and  $l$  is the angular momentum number. We now define  $r_{\max}$  as the value of the radial coordinate at which the effective potential attains its maximum, that is,  $V'_{\text{eff}}(r_{\max}) = 0$  and  $V''_{\text{eff}}(r_{\max}) < 0$ . This value depends on  $l$ , hence  $r_{\max} \equiv r_{\max}(l)$ . We then define  $V_n(l) = V_{\text{eff}}^{(n)}[r_{\max}(l)]$ , which is the  $n$ -th derivative of the effective potential evaluated at  $r_{\max}$ . We also define

$$\alpha(l) = \sqrt{2} \sqrt{-V_2(l)}, \quad (\text{A4})$$

$$\Gamma_1(l) = \frac{1}{\alpha(l)} \left[ \frac{V_4(l)}{8V_2(l)} - \frac{5V_3^2(l)}{24V_2^2(l)} \right], \quad (\text{A5})$$

$$\Gamma_2(l) = \frac{1}{\alpha^3(l)} \left[ \frac{V_3(l)V_5(l)}{48V_2^2(l)} - \frac{V_4^2(l)}{288V_2^2(l)} - \frac{5V_3^2(l)V_4(l)}{576V_2^3(l)} + \frac{5V_3^4(l)}{3456V_2^4(l)} \right], \quad (\text{A6})$$

$$\Gamma(l) = \Gamma_1(l) + \Gamma_2(l), \quad (\text{A7})$$

$$\omega = \sqrt{\Gamma(l) - i \left( n + \frac{1}{2} \right) \alpha(l) + V_0(l)}, \quad (\text{A8})$$

$$\omega_R = \text{Re}[\omega], \quad \& \quad \omega_I = \text{Im}[\omega]. \quad (\text{A9})$$

The Taylor series for the effective potential are

$$V_{\text{eff}}(r \gg 1) \sim \frac{2\Lambda^2 r^2}{9} - \frac{1}{3}\Lambda(2k + l^2 + l) + \frac{\Lambda m}{3r} + O\left(\left(\frac{1}{r}\right)^2\right); \quad (\text{A10})$$

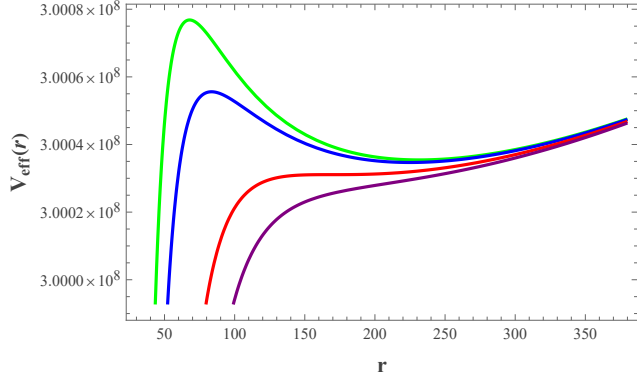
$$V_{\text{eff}}(r \ll 1) \sim -\frac{2(e^{-2\gamma}\eta^2 q^4)}{r^6} + \frac{3e^{-\gamma}\eta m q^2}{r^5} + O\left(\frac{1}{r^4}\right). \quad (\text{A11})$$

We can see that the potential tends to infinity in the limit  $r \rightarrow \infty$ , and tends to minus infinity in the limit  $r \rightarrow 0$ . Here we use values of  $l \in [30000, 50000]$ ,  $M = \{45, 55, 89.96857502, 120\}$  and  $q = 1$ ,  $\gamma = 0.2$ ,  $\Lambda = -1$ ,  $k = 1$ , and  $\eta = -1$ . For these values, the effective potential vanishes at the event horizon. In Fig. 21, we show the effective potential for these parameter values, with  $l = 30000$ . The green ( $m = 45$ ) and blue ( $m = 55$ ) curves possess a maximum and a minimum, whereas the red ( $m = m_{\text{crit}} = 89.96857502$ ) and purple ( $m = 120$ ) curves have no extrema. This also occurs for AdS solutions in general, as shown in Fig. 1 of Ref. [141]. However, the difference here is that  $r_{H(\text{crit})}/L = 3.64367$  instead of  $r_{H(\text{crit})}/L = 1$  ( $r_{H(\text{crit})}$  is the critical value at which  $V_{\text{eff}}$  ceases to possess extrema, and  $L = \sqrt{3/(-\Lambda)}$ ).

We have performed the numerical computation of  $\{r_{\max}(l), V_{\text{eff}}[r_{\max}(l)], \text{Re}[\omega], \text{Im}[\omega]\}$  as functions of  $l$ , and we present the results in Table III and graphically in Fig. 22. We obtain only negative and decreasing values for the imaginary part of the quasinormal frequency, and positive and increasing values for the real part. This indicates the linear stability of the scalar QNMs under a small perturbation of the geometry of the ModAMax solution for  $k = +1$ .

---

[1] M. Visser, Lorenzian Wormholes: from Einstein to Hawking, Springer Verlag, New York (1996).

FIG. 21: Effective potential for the ModAMax solution with  $k = +1$ .

$l$	$r_{max}$	$V_{eff}(r_{max})$	$Re[\omega]$	$Im[\omega]$
30000	67.8799886113	300076829.3184200000	17322.7258050896	-0.0001854857
32000	67.8358974080	341419895.7126960000	18477.5511286696	-0.0001860350
34000	67.7995735533	385430213.8491210000	19632.3766734706	-0.0001864884
36000	67.7692841279	432107783.7024550000	20787.2024020158	-0.0001868671
38000	67.7437562486	481452605.2540950000	21942.0282848695	-0.0001871866
40000	67.7220372830	533464678.4900750000	23096.8542985836	-0.0001874588
42000	67.7034024181	588144003.3997450000	24251.6804242443	-0.0001876926
44000	67.6872920356	645490579.9748650000	25406.5066464242	-0.0001878949
46000	67.6732683530	705504408.2089760000	26561.3329524125	-0.0001880711
48000	67.6609848278	768185488.0969610000	27716.1593316408	-0.0001882256
50000	67.6501641878	833533819.6347150000	28870.9857752494	-0.0001883617

TABLE III: Table of scalar quasinormal modes for the ModAMax solution with  $k = +1$ ,  $l = 30000$ , and  $n = 0$ .

- [2] R. R. Caldwell, M. Kamionkowski, and N. N. Weinberg, Phys. Rev. Lett. 91 (2003) 071301.
- [3] A. Einstein, and N. Rosen, Phys. Rev. 48 (1935) 73.
- [4] K. A. Bronnikov, et al., Int. J. Mod. Phys. D 17 (2008) 25.
- [5] G. Clement, J. C. Fabris, and M. E. Rodrigues, Phys. Rev. D 79 (2009) 064021.
- [6] D. F. Jardim, M. E. Rodrigues, and S. J. M. Houndjo, Eur. Phys. J. Plus 127 (2012) 123.
- [7] K. A. Bronnikov, and J. C. Fabris, Phys. Rev. Lett. 96 (2006) 251101.
- [8] M. Azreg-Aïnou, G. Clement, J. C. Fabris, and M. E. Rodrigues, Phys. Rev. D 83 (2011) 124001.
- [9] M. Azreg-Aïnou, Phys. Rev. D 87 (2013) 024012.
- [10] A. Nakonieczna, M. Rogatko, and R. Moderski, Phys. Rev. D 86 (2012) 044043.
- [11] G. N. Gulychev, and I. Z. Stefanov, Phys. Rev. D 87 (2013) 063005.
- [12] S. Chen, and J. Jing, Class. Quantum Gravit. 30 (2013) 175012.
- [13] K. A. Bronnikov, et al., Phys. Rev. D 89 (2014) 107501.
- [14] M. E. Abishev, et al., Class. Quantum Gravit. 32 (2015) 165010.
- [15] H. Huang, and J. Yang, Phys. Rev. D 100 (2019) 124063.
- [16] M. Azreg-Aïnou, A. K. Ahmed, and M. Jamil, Class. Quantum Gravit. 35 (2018) 235001.
- [17] B. Eslam Panah, and M. E. Rodrigues, Eur. Phys. J. C 83 (2023) 237.
- [18] M. E. Rodrigues, and M. V. d. S. Silva, Phys. Rev. D 107 (2023) 044064.
- [19] B. Podolsky, Phys. Rev. 62 (1942) 68.
- [20] F. Bopp, Ann. Phys. 430 (1940) 345.
- [21] A. Proca, J. Phys. Radium. 7 (1936) 347.
- [22] A. Cadene, Phys. Rev. A 88 (2013) 043815.
- [23] M. Born, and L. Infeld, Proc. R. Soc. A 144 (1934) 425.
- [24] W. Heisenberg, and H. Euler, Z. Phys. 98 (1936) 714.
- [25] B. Hoffmann, Phys. Rev. 47 (1935) 877.
- [26] P. N. Akmansoy, and L. G. Medeiros, Eur. Phys. J. C 78 (2018) 143.
- [27] H. J. Mosquera Cuesta, and G. Lambiase, Phys. Rev. D 80 (2009) 023013.
- [28] H. J. Mosquera Cuesta, and G. Lambiase, JCAP 1103 (2011) 033.

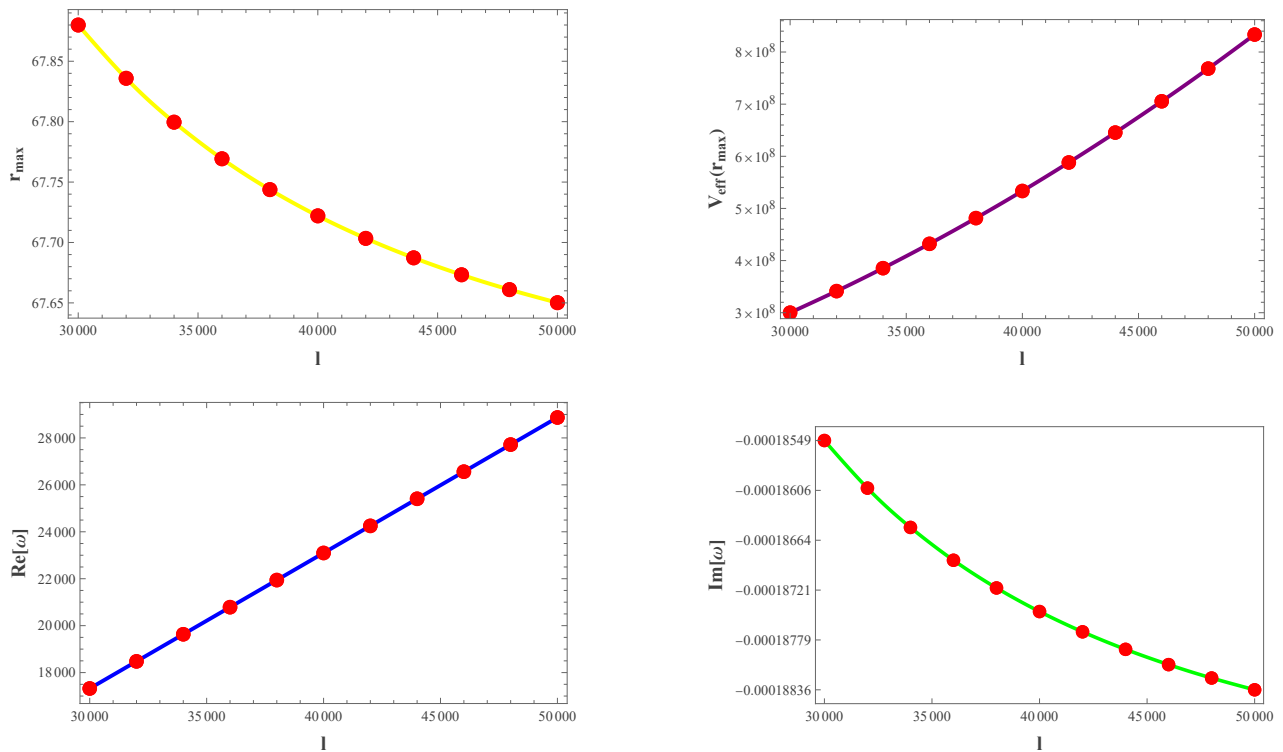


FIG. 22: Graphical representation of  $\{ r_{\max}(l), V_{\text{eff}}[r_{\max}(l)], \text{Re}[\omega], \text{Im}[\omega] \}$  as functions of  $l$ , for the ModAMax solution with  $k = +1$ .

- [29] V. A. De Lorenci, et al., Phys. Rev. D 88 (2013) 065015.
- [30] H. J. Mosquera Cuesta, G. Lambiase, and J. P. Pereira, Phys. Rev. D 95 (2017) 025011.
- [31] V. A. De Lorenci, and J. P. Pereira, Phys. Rev. A 89 (2014) 043822.
- [32] V. I. Denisov, et al., Eur. Phys. J. C 76 (2016) 612.
- [33] L. Campanelli, et al., Phys. Rev. D 77 (2008) 043001.
- [34] P. N. Akmansoy, and L. G. Medeiros, Phys. Lett. B 738 (2014) 317.
- [35] M. Novello, S. E. Perez Bergliaffa, and J. Salim, Phys. Rev. D 69 (2004) 127301.
- [36] PVLAS Collaboration, *Polarizzazione del Vuoto by LASERs* experiment, <https://inspirehep.net/literature?collaboration=PVLAS> (accessed July 2020).
- [37] P. Arias, et al., Phys. Rev. D 82 (2010) 115018.
- [38] R. Battesti, et al., Eur. Phys. J. D 46 (2008) 323.
- [39] O. J. Pike, et al., Nature Photonics. 8 (2014) 434.
- [40] *X-ray Free Electron LASER (XFELs)*, University of Nebraskaâ€“Lincoln, available at <https://unlcms.unl.edu/physics-astronomy/fuchs-group/x-ray-free-electron-laser-xfel> (accessed July 2020).
- [41] *Extreme Light Infrastructure (ELI)*, available at <https://eli-laser.eu/> (accessed July 2020).
- [42] *Shanghai Ultra-Laser Facilities (SULF)*, available at <http://ocs.ciemat.es/EPS2018ABS/pdf/P4.2033.pdf> (accessed July 2020).
- [43] I. Bandos, K. Lechner, D. Sorokin, and P. K. Townsend, Phys. Rev. D 102 (2020) 121703.
- [44] B. P. Kosyakov, Phys. Lett. B 810 (2020) 135840.
- [45] S. I. Kruglov, Int. J. Mod. Phys. 31 (2022) 2250025.
- [46] J. Barrientos, A. Cisterna, M. Hassaine, and K. Pallikaris, Phys. Lett. B 860 (2025) 139214.
- [47] J. Barrientos, A. Cisterna, D. Kubiznak, and J. Oliva, Phys. Lett. B 834 (2022) 137447.
- [48] N. Heidari, and B. Eslam Panah, Phys. Lett. B 866 (2025) 139530.
- [49] T. Hale, D. Kubiznak, J. Mensikova, R. B. Mann, and J. Yang, Phys. Rev. D 111 (2025) 104004.
- [50] B. Eslam Panah, Contrib. Sci. Tech Eng. 1(3) (2024) 25.
- [51] R. C. Pantig, L. Mastrototaro, G. Lambiase, and A. Ovgun, Eur. Phys. J. C 82 (2022) 1155.
- [52] B. Eslam Panah, A. Rincon, and N. Heidari, [arXiv:2411.02907].
- [53] E. Guzman-Herrera, and N. Breton, JCAP 01 (2024) 041.
- [54] B. Eslam Panah, B. Hazarika, and P. Phukon, Prog. Theor. Exp. Phys. 2024 (2024) 083E02.
- [55] K. Jafarzade, Z. Bazyar, and M. Jamil, Phys. Lett. B 864 (2025) 139390.
- [56] B. Eslam Panah, Prog. Theor. Exp. Phys. 2024 (2024) 023E01.
- [57] B. Eslam Panah, Phys. Lett. B 868 (2025) 139711.

[58] Y. Sekhmani, et al., [arXiv:2507.19088].

[59] F. Ahmed, A. Al-Badawi, and I. Sakalli, [arXiv:2508.03226].

[60] Y. Sekhmani, et al., [arXiv:2509.16782].

[61] D. Flores-Alfonso, B. A. Gonzalez-Morales, R. Linares, and M. Macea, Phys. Lett. B 812 (2021) 136011.

[62] I. Bandos, K. Lechner, D. Sorokin, and P. K. Townsend, JHEP 03 (2021) 022.

[63] S. I. Kruglov, Phys. Lett. B 822 (2021) 136633.

[64] S. M. Kuzenko, and E. S. N. Raptakis, Phys. Rev. D 104 (2021) 125003.

[65] Z. Avetisyan, O. Evnin, and K. Mkrtchyan, Phys. Rev. Lett. 127 (2021) 271601.

[66] P. A. Cano, and A. Murcia, JHEP 08 (2021) 042.

[67] A. Ballon Bordo, D. Kubiznak, and T. Perche, Phys. Lett. B 817 (2021) 136312.

[68] A. Bokulic, I. Smolic, and T. Juric, Phys. Rev. D 103 (2021) 124059.

[69] H. Babaei-Aghbolagh, et al., Phys. Lett. B 829 (2022) 137079.

[70] C. A. Escobar, and R. Linares, Phys. Rev. D 106 (2022) 036027.

[71] J. Barrientos, A. Cisterna, D. Kubiznak, and J. Oliva, Phys. Lett. B 834 (2022) 137447.

[72] R. C. Pantig, L. Mastrototaro, G. Lambiase, and A. Ovgun, Eur. Phys. J. C 82 (2022) 1155.

[73] A. Bokulic, T. Juric, and I. Smolic, Phys. Rev. D 106 (2022) 064020.

[74] K. Lechner, P. Marchetti, A. Sainaghi, and D. P. Sorokin, Phys. Rev. D 106 (2022) 016009.

[75] M. Ortaggio, Eur. Phys. J. C 82 (2022) 1056.

[76] H. Nastase, Phys. Rev. D 105 (2022) 105024.

[77] A. Ali, and K. Saifullah, Annals Phys. 437 (2022) 168726.

[78] J. B. Jimenez, D. Bettoni, and P. Brax, JHEP 02 (2023) 009.

[79] C. Ferko, and A. Gupta, Phys. Rev. D 108 (2023) 046013.

[80] S. M. Kuzenko, and I. N. McArthur, JHEP 05 (2023) 127.

[81] H. Rathi, and D. Roychowdhury, JHEP 07 (2023) 026.

[82] H. M. Siahaan, Int. J. Mod. Phys. D 32 (2023) 2350099.

[83] H. M. Siahaan, Commun. Theor. Phys. 76 (2024) 065402.

[84] S. W. Hawking, and G. F. Ellis, *The large scale structure of spacetime*, Cambridge University Press, Cambridge, England, (1973).

[85] S. W. Hawking, Commun. Math. Phys. 25 (1972) 152.

[86] J. P. S. Lemos, Phys. Lett. B 353 (1995) 46.

[87] R. G. Cai, and Y. Z. Zhang, Phys. Rev. D 54 (1996) 4891.

[88] D. R. Brill, J. Louko, and P. Peldan, Phys. Rev. D 56 (1997) 3600.

[89] R. G. Cai, J. Y. Ji, and K. S. Soh, Phys. Rev. D 57 (1998) 6547.

[90] S. Hajkhalili, and A. Sheykhi, Phys. Rev. D 99 (2019) 024028.

[91] M. M. Stetsko, Phys. Rev. D 101 (2020) 104004.

[92] T. Wang, Z. Zhang, X. Kong, and L. Zhao, Nucl. Phys. B. 995 (2023) 116352.

[93] D. Chen, Y. He, and J. Tao, Eur. Phys. J. C 83 (2023) 872.

[94] H. Wang, and Y. Z. Du, Chin. Phys. C 48 (2024) 095109.

[95] J. D. Bekenstein, Phys. Rev. D 7 (1973) 2333; S. W. Hawking, Nature. 248 (1974) 3.

[96] H. Kleinert, Phys. Rev. D 60 (1999) 085001.

[97] H. B. Callen, John Wiley-Sons, Inc., New York, 1985.

[98] A. L. Greer, Science. 267 (1995) 1947.

[99] D. C. Zou, Y. Liu, and R. Yue, Eur. Phys. J. C 77 (2017) 365.

[100] D. Layzer, Oxford Univ. Press, (1991).

[101] J. M. Maldacena, Adv. Theor. Math. Phys. 2 (1998) 231.

[102] E. Witten, Adv. Theor. Math. Phys. 2 (1998) 253.

[103] D. Kubiznak, R. B. Mann, and M. Teo, Class. Quantum Grav. 34 (2017) 063001.

[104] D. Kastor, S. Ray, and J. Traschen, Class. Quantum Grav. 26 (2009) 195011.

[105] O. Okcu, and E. Aydiner, J. Eur. Phys. J. C 77 (2017) 24.

[106] C. V. Johnson, Entropy. 18 (2016) 120.

[107] H. Ghaffarnejad, E. Yaraie, and M. Farsam, Int. J. Theor. Phys. 57 (2018) 1671.

[108] J. X. Mo, G. Q. Li, S. Q. Lan, and X. B. Xu, Phys. Rev. D 98 (2018) 124032.

[109] O. Okcu, and E. Aydiner, Eur. Phys. J. C 78 (2018) 123.

[110] Z. W. Zhao, Y. H. Xiu, and N. Li, Phys. Rev. D 98 (12) (2018) 124003.

[111] S. Q. Lan, Phys. Rev. D 98 (2018) 084014.

[112] J. X. Mo, and G. Q. Li, Class. Quantum Grav. 37 (2020) 045009.

[113] X. M. Kuang, B. Liu, and A. Ovgun, Eur. Phys. J. C 78 (2018) 840.

[114] M. R. Setare, H. Adami, Phys. Rev. D 91 (2015) 084014.

[115] A. Belhaj, et al., J. High Energy Phys. 2015 (2015) 149.

[116] E. Caceres, P. H. Nguyen, and J. F. Pedraza, J. High Energy Phys. 2015 (2015) 184.

[117] M. Zhang, W. B. Liu, Int. J. Theor. Phys. 55 (2016) 5136.

[118] J. X. Mo, F. Liang, and G. Q. Li, J. High Energy Phys. 2017 (2017) 10.

[119] R. A. Hennigar, F. McCarthy, A. Ballon, and R. B. Mann, Class. Quantum Gravity 34 (2017) 175005.

[120] C. Bhamidipati, and P. K. Yerra, Eur. Phys. J. C 77 (2017) 534.

- [121] J. X. Mo, G. Q. Li, J. High Energy Phys. 2018 (2018) 122.
- [122] S. H. Hendi, B. Eslam Panah, S. Panahiyan, H. Liu, and X. H. Meng, Phys. Lett. B 781 (2018) 40.
- [123] B. Eslam Panah, Kh. Jafarzade, and S. H. Hendi, Nucl. Phys. B 961 (2020) 115269.
- [124] A. Ashtekar, and A. Magnon, Class. Quantum Gravit. 1 (1984) L39.
- [125] A. Ashtekar, and S. Das, Class. Quantum Gravit. 17 (2000) L17.
- [126] T. Regge, and J. A. Wheeler, Phys. Rev. 108 (1957) 1063.
- [127] F. J. Zerilli, Phys. Rev. Lett. 24 (1970) 737.
- [128] V. Moncrief, Annals of Physics. 88 (1974) 323.
- [129] H. Kodama, and A. Ishibashi, Prog. Theor. Phys. 110 (2003) 701.
- [130] H. Kodama, and A. Ishibashi, Prog. Theor. Phys. 111 (2004) 29.
- [131] S. Chandrasekhar, *The Mathematical Theory of Black Holes*, Oxford University Press (1983).
- [132] K. D. Kokkotas, and B. Schmidt, Living Rev. Relativity. 2 (1999) 2.
- [133] G. Dotti, and R. Gleiser, Phys. Rev. D 72 (2005) 044018.
- [134] B. F. Schutz, and C. M. Will, Astrophys. J. 291 (1985) L33.
- [135] S. Iyer, and C. M. Will, Phys. Rev. D 35 (1987) 3621.
- [136] R. A. Konoplya, Phys. Rev. D 68 (2003) 024018.
- [137] R. A. Konoplya, and A. Zhidenko, Rev. Mod. Phys. 83 (2011) 793.
- [138] B. Wang, C. -Y. Lin, and E. Abdalla, Phys. Lett. B 481 (2000) 79.
- [139] E. Berti, and K. D. Kokkotas, Phys. Rev. D 67 (2003) 064020.
- [140] G. Festuccia, and H. Liu, Adv. Sci. Lett. 2 (2009) 221.
- [141] E. Berti, V. Cardoso, and P. Pani, Phys. Rev. D 79 (2009) 101501.
- [142] E. Berti, V. Cardoso, and A. O. Starinets, Class. Quantum Gravit. 26 (2009) 163001.